Projection-based embedded discrete fracture model (pEDFM) for flow and heat transfer in real-field geological formations with hexahedral corner-point grids

Mousa HosseiniMehr [a], Janio Piguave Tomala [a], Cornelis Vuik [a], Mohammed Al Kobaisi [b], Hadi Hajibeygi [a,*]

[a] *Delft University of Technology, P.O. Box 5048, 2600 GA Delft, The Netherlands*
[b] *Khalifa University of Science and Technology, P.O. Box 2533, Abu Dhabi, United Arab Emirates*

ARTICLE INFO

ABSTRACT

We present the projection-based embedded discrete fracture model (pEDFM) for hexahedral corner-point grid (CPG) geometries, for the simulation of hydrothermal processes in fractured porous media. Unlike the previously-developed pEDFM for structured box grids, our new development allows for the modeling of complex geometries defined with hexahedral CPG cells. It also advances the pEDFM method to include coupled flow and heat transfer systems. Mass and energy conservation equations are simulated in a fully-coupled manner using a fully-implicit (FIM) integration scheme. This allows for stable simulations, specially when large time steps are taken. Independent corner-point grids are imposed on the rock matrix and all fractures, with conductivities ranging from highly permeable to flow barriers. The connectivities between the non-neighboring grid cells are described such that a consistent discrete representation of the embedded fractures occurs within the corner-point grid geometry, specially as the quadrilateral interfaces are allowed to be fully flexible. Various numerical tests including geologically-relevant and real-field models, which are established in the literature, are conducted to demonstrate the applicability of the developed method. It is shown that pEDFM can accurately capture the physical influence of both highly conductive fractures and flow barriers on the flow and heat transfer fields in complex reservoir geometries. This development is promising for flow simulations of real-field geo-models, increasing the discretization flexibility and enhancing the computational performance for capturing explicit fractures accurately.

1. Introduction

For successful development of a variety of geo-engineering applications related to geo-energy (e.g., hydrocarbon and geothermal) production and storage (e.g., CO_2 storage and hydrogen storage), a detailed understanding of fluid mass and heat transport in porous rocks is essential. To achieve this, accurate and efficient simulation of mass and heat transfer in the subsurface geological formation plays a crucial role. Computer models and their resulting estimation of the dynamic processes contribute to efficient and safe operations in the production or storage facilities for any of the above-listed applications. Simulation results provide valuable insights into the optimization of hydrocarbon extractions (Jansen et al., 2005), the energy production outlines and the life-time of geothermal systems (OSullivan et al., 2001; Axelsson et al., 2003; Burnell et al., 2012, 2015), the practical capacities that can be

offered by the underground formations to store CO_2 (Eiken et al., 2011; Class et al., 2009; Harris et al., 2021; Wang et al., 2021; Ruprecht et al., 2014) or hydrogen (Anon, 2021; Heinemann et al., 2021), and many more.

However, while modeling subsurface flow, the geo-engineering community faces a number of key challenges. The geological formations are often large scales in nature. While they are located only a few kilometers deep in the subsurface (crust) and have a thickness of hundreds (if not tens) of meters, their areal extents can easily be in orders of kilometers. In order to reflect the geological and geometrical properties of the subsurface accurately, high-resolution computational grids are often imposed on the domain. This results in significant computational complexity, which makes it impossible to run the computer models using conventional methods. Moreover, strong spatial heterogeneity

contrasts are observed between various physical and chemical properties in the formations. These heterogeneities affect the flow and transport properties of the rock (i.e., storage capacity and conductivity) across several orders of magnitude. The discretization of the governing partial differential equations, or PDEs, results in ill-conditioned linear systems of equations creating challenges for the numerical solution schemes applied to solve such heterogeneous systems. In addition, the measurement of the heterogeneous properties several kilometers beneath the subsurface involves a great deal of uncertainty. In order to minimize the impact of such uncertainties, instead of one realization, hundreds (if not thousands) of realizations are created in the context of uncertainty quantification (UQ) and a large number of simulations have to be run. Thus, the complexity of the system can have a huge impact on providing predictions on a reasonable time scale.

Furthermore, geological formations are often defined with complex geometry and stratigraphy. Using Cartesian grid geometry, even though it allows for simpler conceptual modeling analyses, can result in oversimplified and inaccurate predictions. In addition, the presence of faults and fractures has significant effects on fluid and heat flow patterns through the subsurface formations. The heterogeneity contrasts in the length scales and conductivities caused by these complex networks of fractures and faults can cause extreme challenges in solving the linear systems using numerical methods (Gan and Elsworth, 2016; Gholizadeh Doonechaly et al., 2016b; Salimzadeh et al., 2019). Moreover, the strong coupling of mass and heat transport results in severe non-linearity which negatively impacts the stability and convergence in the system. In case of multi-phase flow (e.g., high-enthalpy geothermal systems) these issues become more drastic (Wong et al., 2018). The elastic and plastic deformations in the geo-mechanical interactions (Rossi et al., 2018; Garipov et al., 2016; Gholizadeh Doonechaly et al., 2016a), reactive transport (e.g., geo-chemical interaction between the substances) (Morel and Morgan, 1972; Leal et al., 2017; Salimzadeh and Nick, 2019) and compositional alterations in the fluid and rock are among the list of other noteworthy challenges. Therefore, there is a high demand for developing advanced simulation methods that are computationally efficient and scalable, yet accurate at the desired level. Consequently, the development of a reliable computer model for simulation of subsurface flow and transport in fractured porous media is critical to address the challenges in practical applications. As a result, many advanced numerical methods have been developed.

To represent the real-field geological formations accurately, instead of using Cartesian grids, more complex and flexible gridding structures are needed as these formations are more conveniently represented by flexible grids (Lie et al., 2020; Reichenberger et al., 2006). The grid geometry should create a set of discrete cell volumes that approximate the reservoir volume, yet fit the transport process physics, and avoid over complications as much as possible (Ahmed et al., 2015). Unstructured grids allow for many flexibilities, which need to be carefully applied to a computational domain so that the discrete systems do not become over-complex (Karimi-Fard et al., 2004; Jiang and Younis, 2016). Without introducing the full flexibility (and at the same time complexity) of the fully unstructured grids, the corner-point grid (CPG) geometry allows for many possibilities with better representation of the geological structures. This has made CPG attractive in the geoscience industry-grade simulations (Ponting, 1989; Ding and Lemonnier, 1995; GeoQuest, 2014; Lie, 2019).

Fractures have often small apertures (size of millimeters) but pose a serious impact on flow patterns due to large contrast of permeability between fractures and their neighboring rock matrix (Berkowitz, 2002; Kumar et al., 2020). Therefore, consistent representation of these geological features is important in predicting the flow behavior using numerical simulations (Berkowitz, 2002). Different approaches have been proposed to model the effect of fractures on flow patterns. To avoid direct numerical simulation (DNS) and thereby imposing extremely high resolution grids on the length scales of fracture apertures,

it is possible to upscale fractures by obtaining averaged and effective properties (e.g., permeability) between fractures (or faults) and the hosting rock (also known as the rock matrix). This introduces a porous media representation without fractures but with approximated conductivities. However, such models raise concerns about the inaccuracy of the simulation results due to the employed excessively upscaled parameters, especially in presence of high conductivity contrasts between the matrix and fractures. Therefore, two distinct methods have been introduced in fracture modeling approaches; the so-called dual continuum models (also known as dual porosity or dual porosity-dual permeability) (Warren and Root, 1963; Barenblatt et al., 1983; Kazemi et al., 1996) and the discrete fracture model (DFM) (Dietrich et al., 2005). In the dual porosity method, the matrix plays the role of fluid storage and the fluid only flows inside the fractures as it is assumed that there is no direct connection between the matrix cells. In the dual porosity-dual permeability method, both matrix and fracture have connections. Both dual porosity and dual porosity-dual permeability models homogenize the fracture domain in a computing block and neglect specific fracture features such as orientation and size. DFM, on the other hand, considers fractures as a separate system in a lower dimensional domain than that of the rock matrix, and couples them through a flux transfer function. In 2D domains the fractures are represented by 1D line-segments and in 3D domains each fracture is modeled by a 2D plane-segment. DFM methods have been developed and evolved quite significantly during the past several years (See, e.g., (Karimi-Fard et al., 2004; Lee et al., 1999, 2001; Li and Lee, 2008; Ahmed et al., 2015; Geiger-Boschung et al., 2009; Karvounis, 2013; Reichenberger et al., 2006; Moinfar et al., 2014; Fumagalli et al., 2016), and the references therein). Two different DFM approaches have been presented in the literature: the Embedded DFM (EDFM) and the Conforming DFM (CDFM) (Flemisch et al., 2018; Li and Voskov, 2021; Moinfar et al., 2013). The main difference between these two techniques resides in the flexibility to the grid geometry (Shah et al., 2016). In CDFM, the fracture elements are located at the interfaces between the unstructured matrix grid-cells (Sandve et al., 2012). The effect of the fractures is represented by modifying transmissibilities at those interfaces. Therefore, there is an accurate consideration of flux transfer between the matrix and the fractures (Karimi-Fard et al., 2004; Reichenberger et al., 2006; Ahmed et al., 2015). However for highly dense fracture networks the number of matrix grid cells should be very high with very fine grid cells close to the fracture intersections, to account for the fractures. In addition, in case of fracture generation and propagation, the matrix grid has to be redefined at various steps of the simulation which reduces the efficiency of such an approach. All of these complexities can limit the application of CDFM in real-field applications. In EDFM, fractures are discretized separately and independently from the matrix on a lower dimensional domain by using non-conforming grids (Lee et al., 1999; Li and Lee, 2008). Once the grid cells are created and the discretization is finished, the fractures and matrix are coupled together using conservative flux transfer terms that calculate the flow between each fracture element and its overlapping neighbors (Hajibeygi et al., 2011; HosseiniMehr et al., 2018; Xu and Sepehrnoori, 2019). Having two independent grids allows for the modeling of complex fracture networks with simpler grids for the matrix.

While EDFM can provide acceptable results for highly conductive fractures, it cannot accurately represent flow barriers (such as non-conductive fractures and sealing faults). To resolve this limitation, projection-based EDFM (pEDFM) was introduced, for the first time, by Tene et al. (2017) and extended to multilevel multiscale framework in a fully 3D Cartesian geometry (HosseiniMehr et al., 2020). pEDFM provides consistent connectivity values between the rock matrix and the fractures, and thus can be applied to fractured porous media with any range of conductivity contrasts between the rock and the fractures (either highly conductive or impermeable). The original pEDFM concept (Tene et al., 2017) has been applied to more geoscientific applications (e.g. in (Jiang and Younis, 2017)).

In this work, the projection-based embedded discrete fracture model (pEDFM) on the corner-point grid (CPG) geometry is presented. To cover a more general application criteria, different flow environments are considered, i.e., multiphase fluid flow model (isothermal) in fractured porous media and single-phase coupled mass-heat flow in low-enthalpy fractured geothermal reservoirs. The finite volume method (FVM) is used for discretization of the continuum domain. To represent realistic and geologically relevant domains, the corner-point grid geometry is used. The sets of nonlinear equations are coupled using fully-implicit (FIM) coupling strategy. The flux terms in the mass and energy conservation equations are discretized with an upwind two-point flux approximation (TPFA) in space and with a backward (implicit) Euler scheme in time. The pEDFM is employed in order to explicitly and consistently represent fractures and to provide computational grids for the rock matrix and the fractures independently regardless of the complex geometrical shape of domain. Here, the applicability of the pEDFM implementation (Tene et al., 2017; HosseiniMehr et al., 2020) has been extended to include fractures with generic conductivity contrasts (either highly conductive or impermeable) with any positioning and orientation on the corner-point grid geometry. This matter is paramount for practical field-scale applications. In addition to geometrical flexibility of EDFM, the matrix–matrix and fracture–matrix connectivities are altered to consider the projection of fractures on the interfaces of matrix grid cells. Using various synthetic and geologically-relevant real-field models the performance of the pEDFM on the corner-point grid geometry is shown.

This article is structured as follows: First, the governing equations are described in Section 2. The discretization and simulation strategy are explained in Appendix A.3. In Section 4, the corner-point grid geometry and calculation of the transmissibilities are briefly covered. The pEDFM approach for the corner-point grid geometry is presented in Section 5. The test cases and the numerical results are shown in Section 6. At last, the paper is concluded in Section 7.

2. Governing equations

In this section, the governing equations of the isothermal multiphase flow is revisited. In order to improve the readability, the governing equations for single-component (water) two-phase (vapor–liquid) coupled mass-heat transport in geothermal systems are presented in the appendix.

Mass conservation in porous media for phase α in the absence of mass-exchange between the phases, capillary and gravitational effects with n_{frac} explicit fractures is given as

$$\frac{\partial}{\partial t}\left(\phi \rho_\alpha S_\alpha\right)^m - \nabla \cdot \left(\rho_\alpha \lambda_\alpha \cdot \nabla p\right)^m =$$
$$\rho_\alpha q_\alpha^{m,w} + \sum_{i=1}^{n_{\text{frac}}} \rho_\alpha Q_\alpha^{m,f_i} \quad \text{on} \quad \Omega_m \subseteq \mathbf{R}^n, \tag{1}$$

for the rock matrix m and

$$\frac{\partial}{\partial t}\left(a\,\phi \rho_\alpha S_\alpha\right)^{f_i} - \nabla \cdot \left(a\,\rho_\alpha \lambda_\alpha \cdot \nabla p\right)^{f_i} =$$
$$\rho_\alpha q_\alpha^{f_i,w} + \rho_\alpha Q_\alpha^{f_i,m} + \sum_{j=1}^{n_{\text{frac}}} \left(\rho_\alpha Q_\alpha^{f_i,f_j}\right)_{j \neq i}$$
$$\text{on} \quad \Omega_{f_i} \subseteq \mathbf{R}^{n-1} \quad \forall i \in \{1, \ldots, n_{\text{frac}}\} \tag{2}$$

for the lower-dimensional fracture f_i with aperture a. There exist n_α phases. Moreover, the superscripts m, f and w in Eqs. (1)–(2) indicate, respectively, the rock matrix, the fractures and the wells. Here, ϕ is the porosity of the medium, ρ_α, S_α, λ_α are the density, saturation, and mobility of phase α, respectively. In addition, $\lambda = \frac{k_{r_\alpha}}{\mu_\alpha}\mathbf{K}$ holds, where k_r, μ and $\mathbf{K}$ are phase relative permeability, viscosity and rock absolute permeability tensor, respectively. Also, q_α is the phase source term (i.e., wells). Finally, Q_α^{m,f_i} and $Q_\alpha^{f_i,m}$ are the phase flux exchanges between matrix and the ith fracture, whereas $Q_\alpha^{f_i,f_j}$ represents the

influx of phase α from jth fracture to the ith fracture. Note that the mass conservation law enforces $\iiint_V Q_\alpha^{m,f_i} dV = -\iint_{A_{f_i}} Q_\alpha^{f_i,m} dA$ and $\iint_{A_{f_i}} Q_\alpha^{f_i,f_j} dA = -\iint_{A_{f_j}} Q_\alpha^{f_j,f_i} dA$.

The Peaceman well model (Peaceman, 1978) is used to obtain the well source terms of each phase for the rock matrix as

$$q_\alpha^{m,w} = \frac{WI \cdot \lambda_\alpha^* \cdot (p^w - p^m)}{\Delta V} \tag{3}$$

and for the fractures as

$$q_\alpha^{f_i,w} = \frac{WI \cdot \lambda_\alpha^* \cdot (p^w - p^{f_i})}{\Delta A}. \tag{4}$$

Here, WI denotes the well productivity index and λ_α^* is the effective mobility of each phase ($\lambda = \frac{k_{r_\alpha}}{\mu_\alpha} K$) between the well and the grid cell penetrated by the well in each medium. In the discrete system for the rock matrix, the control volume is defined as ΔV and in the discrete system for the fracture, the control area is written as ΔA.

The flux exchange terms Q_α^{m,f_i}, $Q_\alpha^{f_i,m}$ (matrix–fracture connectivities) and $Q_\alpha^{f_i,f_j}$ (fracture–fracture connectivities) are written as:

$$Q_\alpha^{m,f_i} = CI^{m,f_i} \cdot \lambda_\alpha^* \cdot (p^{f_i} - p^m)$$
$$Q_\alpha^{m,f_i} = CI^{f_i,m} \cdot \lambda_\alpha^* \cdot (p^m - p^{f_i}) \tag{5}$$
$$Q_\alpha^{f_i,f_j} = CI^{f_i,f_j} \cdot \lambda_\alpha^* \cdot (p^{f_j} - p^{f_i}),$$

where CI indicates the connectivity index between each two non-neighboring elements (see Eq. (49)).

Eqs. (1)–(2), subject to proper initial and boundary conditions, form a well-posed system for n_α unknowns, once the $\sum_{\alpha=1}^{n_\alpha} S_\alpha = 1$ constraint is employed to eliminate one of the phase saturation unknowns. Here, this system of equations is solved for a two phase flow fluid model with the primary unknowns of p and S_1 (from now on indicated as S). Please note that the effects of both capillarity (in case of a multiphase flow) and gravity are neglected in all the equations.

3. Discretization of the equations and the simulation strategy

The discretization of the nonlinear equations is done using the finite volume method (FVM). The equations are discretized with a two-point-flux-approximation (TPFA) finite-volume scheme in space and a backward (implicit) Euler scheme in time. Independent structured grids are generated for a three-dimensional (3D) porous rock and 2D fracture planes. The discretization is done for each medium. For a corner-point grid geometry, an illustration is presented in Fig. 4.

The coupled system of non-linear equations (1)–(2) is discretized by calculating the fluxes. The advective TPFA flux of phase α between control volumes i and j reads

$$F_{\alpha,ij} = \rho_\alpha^* \frac{k_{r_\alpha}^*}{\mu_\alpha^*} T_{ij}(p_i - p_j). \tag{6}$$

Here, $T_{ij} = \frac{A_{ij}}{d_{ij}} K_{ij}^H$ denotes the transmissibility between the neighboring cells i and j. A_{ij} and d_{ij} are the interface area and the distance between these two cells centers respectively. The term K_{ij}^H is the harmonic average of the two permeabilities. The superscript $*$ indicates that the corresponding terms are evaluated using a phase potential upwind scheme. Following the EDFM and pEDFM paradigms (Hajibeygi et al., 2011; Tene et al., 2017; HosseiniMehr et al., 2018), the fluxes between a matrix cell i and a fracture cell j are modeled as

$$\mathcal{F}_{\alpha,ij}^{m,f} = -\mathcal{F}_{\alpha,ij}^{f,m} = -\rho_\alpha^* \frac{k_{r_\alpha}^*}{\mu_\alpha^*} T_{ij}^{m,f}(p_i^m - p_j^f), \tag{7}$$

In this equation, $T_{ij}^{m,f}$ is the geometrical transmissibility in the mass flux between cell i belonging to the rock matrix m and the element j belonging to the fracture f_i and it reads:

$$T_{ij}^{m,f} = K_{ij}^H \times CI_{ij}. \tag{8}$$
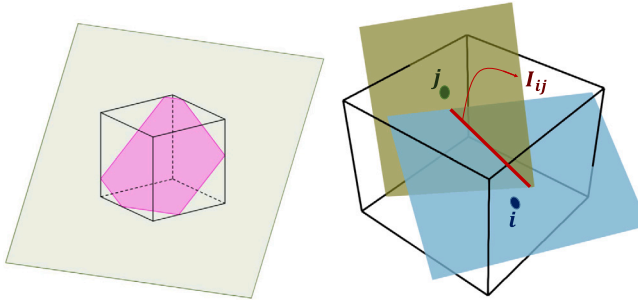
Fig. 1. Visualization of a matrix–fracture overlap and a fracture–fracture intersection. The figure on the left shows a fracture element overlapping with a matrix grid cell. The overlapping section forms an irregular polygon. The figure on the right illustrates intersection of two elements from two fracture plates inside a matrix grid cell with the intersection line colored in red. (For interpretation of the references to color in this figure legend, the reader is referred to the web version of this article.)

In the equation above, K_{ij}^H denotes the harmonically averaged permeability between the rock matrix and the overlapping fracture elements. Moreover, $CI_{ij}^{m,f}$ is the connectivity index between the two overlapping elements. The EDFM and pEDFM model the matrix–fracture connectivity index as:

$$CI_{ij}^{m,f} = \frac{A_{ij}^{m,f}}{\langle d \rangle_{ij}}, \tag{9}$$

with $A_{ij}^{m,f}$ being the area fraction of fracture cell j overlapping with matrix cell i (see Fig. 1, on the left) and $\langle d \rangle_{ij}$ being the average distance between these two cells (Hajibeygi et al., 2011).

Similarly, the flux exchange between intersecting fracture elements i (belonging to fracture f_i) and j (belonging to fracture f_j) is modeled as

$$\mathcal{F}_{\alpha,ij}^{f_i,f_j} = -\mathcal{F}_{\alpha,ij}^{f_j,f_i} = -\rho_\alpha^* \frac{k_{r_\alpha}^*}{\mu_\alpha^*} T_{ij}^{f_i,f_j} (p_i^{f_i} - p_j^{f_j}). \tag{10}$$

Here, $T_{ij}^{f_i,f_j}$ is the geometrical transmissibility in the mass flux between element i in the fracture f_i and the element j in the fracture f_j, which reads:

$$T_{ij}^{f_i,f_j} = K_{ij}^H \frac{CI_{iI_{ij}}^{f_i} \times CI_{jI_{ij}}^{f_j}}{CI_{iI_{ij}}^{f_i} + CI_{jI_{ij}}^{f_j}}. \tag{11}$$

Please note that the geometrical transmissibility $T_{ij}^{f_i,f_j}$ between the two non-neighboring (intersecting) fracture cells is obtained on a lower dimensional formulation. This is needed due to the fact that the intersection between two 2D fracture plates forms a line-segment and the intersection between two 1D fracture line-segments results in a point. Fig. 1 (on the right) visualizes an example of an intersection between two non-neighboring 2D fracture elements. The result of the intersection is a line segment I_{ij} (colored in red) with the average distances from the intersection segment written as $\langle d \rangle_{iI_{ij}}^{f_i} \neq \langle d \rangle_{jI_{ij}}^{f_j}$. This is the reason why these transmissibilities are computed using a harmonic-average formulation as shown above.

Thus, at each time-step the following system of equations is solved

$$\left(\frac{(\phi \rho_\alpha S_\alpha)_i^{n+1} - (\phi \rho_\alpha S_\alpha)_i^n}{\Delta t} \right)^m + \left(\sum_{j=1}^{N_n} F_{\alpha,ij} \right)^m +$$

$$\sum_{k=1}^{n_{\text{frac}}} \left(\sum_{j=1}^{N_{f_k}} \mathcal{F}_{\alpha,ij}^{m,f_k} \right) = \rho_\alpha q_{\alpha,i}^{m,w},$$

$$\forall i \in \{1, \dots, N_m\} \tag{12}$$

in the matrix and

$$\left(\frac{(a \phi \rho_\alpha S_\alpha)_i^{n+1} - (a \phi \rho_\alpha S_\alpha)_i^n}{\Delta t} \right)^{f_h} + \left(\sum_{j=1}^{N_n} F_{\alpha,ij} \right)^{f_h} +$$

$$\sum_{j=1}^{N_m} \mathcal{F}_{\alpha,ij}^{f_h,m} + \sum_{k=1}^{n_{\text{frac}}} \left(\sum_{j=1}^{N_{f_k}} \mathcal{F}_{\alpha,ij}^{f_h,f_k} \right) = \rho_\alpha q_{\alpha,i}^{f_h,w},$$

$$\forall i \in \{1, \dots, N_{f_h}\} \tag{13}$$

in each fracture f_h. Here, N_m and N_{f_k} are the number of cells in the matrix and number of the cells in fracture f_k, respectively. N_n indicates the number of neighboring cells (2 in 1D, 4 in 2D, 6 in 3D).

Eqs. (12)–(13) can be written in residual form as

$$\left(r_{\alpha,i}^{n+1} \right)^m = \rho_\alpha q_{\alpha,i}^{m,w} - \left(\frac{(\phi \rho_\alpha S_\alpha)_i^{n+1} - (\phi \rho_\alpha S_\alpha)_i^n}{\Delta t} \right)^m -$$

$$\left(\sum_{j=1}^{N_n} F_{\alpha,ij} \right)^m - \sum_{k=1}^{n_{\text{frac}}} \left(\sum_{j=1}^{N_{f_k}} \mathcal{F}_{\alpha,ij}^{m,f_k} \right),$$

$$\forall i \in \{1, \dots, N_m\} \tag{14}$$

for the rock matrix, and

$$\left(r_{\alpha,i}^{n+1} \right)^{f_h} = \rho_\alpha q_{\alpha,i}^{f_h,w} - \left(\frac{(a \phi \rho_\alpha S_\alpha)_i^{n+1} - (a \phi \rho_\alpha S_\alpha)_i^n}{\Delta t} \right)^{f_h} -$$

$$\left(\sum_{j=1}^{N_n} F_{\alpha,ij} \right)^{f_h} - \sum_{j=1}^{N_m} \mathcal{F}_{\alpha,ij}^{f_h,m} - \sum_{k=1}^{n_{\text{frac}}} \left(\sum_{j=1}^{N_{f_k}} \mathcal{F}_{\alpha,ij}^{f_h,f_k} \right),$$

$$\forall i \in \{1, \dots, N_{f_h}\} \tag{15}$$

for fracture f_h. Let us define $r^n = [(r^m)^n, (r^{f_1})^n \dots \dots (r^{f_{n_{\text{frac}}}})^n]^T$ where $(r^k)^n$ is the residual vector of medium k at time-step n. Similarly, p^n and S^n indicate the vectors of pressure and saturation unknowns (of all media). The residual r^{n+1} is a non-linear function of the primary unknowns p^{n+1} and S^{n+1}. Thus, at each time-step a Newton–Raphson method is employed to solve the non-linear system iteratively, i.e.

$$r_\alpha^{\nu+1} \approx r_\alpha^\nu + \frac{\partial r_\alpha}{\partial p} \bigg|^\nu \delta p^{\nu+1} + \frac{\partial r_\alpha}{\partial S} \bigg|^\nu \delta S^{\nu+1}, \tag{16}$$

where the superscript ν is the iteration index. Consequently, at each Newton's iteration the linearized system $\mathbf{J}^\nu \delta x^{\nu+1} = -r^\nu$ is solved. Here, $\mathbf{J}^\nu$ is the Jacobian matrix with $\delta x^{\nu+1} = [\delta p, \delta S]^T$. Therefore, assuming two phases (the indices 1 and 2 representing the equations of the first and the second phases respectively), the linear system of equations can be written as

$$\underbrace{\begin{pmatrix} \begin{pmatrix} J_{1,p}^{m,m} & J_{1,p}^{m,f} \\ J_{1,p}^{f,m} & J_{1,p}^{f,f} \end{pmatrix} & \begin{pmatrix} J_{1,S}^{m,m} & J_{1,S}^{m,f} \\ J_{1,S}^{f,m} & J_{1,S}^{f,f} \end{pmatrix} \\ \begin{pmatrix} J_{2,p}^{m,m} & J_{2,p}^{m,f} \\ J_{2,p}^{f,m} & J_{2,p}^{f,f} \end{pmatrix} & \begin{pmatrix} J_{2,S}^{m,m} & J_{2,S}^{m,f} \\ J_{2,S}^{f,m} & J_{2,S}^{f,f} \end{pmatrix} \end{pmatrix}}_{\mathbf{J}^\nu} \underbrace{\begin{pmatrix} \delta p^m \\ \delta p^f \\ \delta S^m \\ \delta S^f \end{pmatrix}^{\nu+1}}_{\delta x^{\nu+1}} = - \underbrace{\begin{pmatrix} r_1^m \\ r_1^f \\ r_2^m \\ r_2^f \end{pmatrix}^\nu}_{r^\nu} \tag{17}$$

In this formulation, non-linear convergence is reached when the following conditions are satisfied:

$$\left(\frac{\|r_1^{\nu+1}\|_2}{\|r_1^0\|_2} < \epsilon_{(r_1)} \quad \vee \quad \frac{\|r_1^{\nu+1}\|_2}{\|rhs_1\|_2} < \epsilon_{(r_1)} \right) \quad \wedge$$

$$\left(\frac{\|r_2^{\nu+1}\|_2}{\|r_2^0\|_2} < \epsilon_{(r_2)} \quad \vee \quad \frac{\|r_2^{\nu+1}\|_2}{\|rhs_2\|_2} < \epsilon_{(r_2)} \right) \quad \wedge$$

$$\left(\frac{\|\delta p\|_2}{\|p\|_2} < \epsilon_{(p)} \quad \wedge \quad \frac{\|\delta S\|_2}{\|S\|_2} < \epsilon_{(S)} \right) \tag{18}$$

Here, $\epsilon_{(r_1)}$, $\epsilon_{(r_2)}$, $\epsilon_{(p)}$ and $\epsilon_{(S)}$, are the user-defined tolerances that are set initially as input at the beginning of the simulation. The notation $\|x\|_2$ is the second norm of the vector x. The superscript 0 denotes the value of its corresponding vector at the initial state of the iteration step. Please note that in some systems the condition $\frac{\|r^{v+1}\|_2}{\|rhs\|_2} < \epsilon_{(r)}$ can result in a better convergence when compared to $\frac{\|r^{v+1}\|_2}{\|r^0\|_2} < \epsilon_{(r)}$ and vice versa. Therefore both conditions are checked and either of them can implicate the convergence signal.

4. Corner-point grid geometry

A corner-point grid (CPG) is defined with a set of straight pillars outlined by their endpoints over a Cartesian mesh in the lateral direction (Lie, 2019). On every pillar, a constant number of nodes (corner-points) is set, and each cell in the grid is set between 4 neighboring pillars and two neighboring points on each pillar. Every cell can be identified by integer coordinates (i, j, k); where the k coordinate runs along the pillars, and i and j coordinates span along each layer. The cells are ordered naturally with the i-index (x-axis) cycling fastest, then the j-index (y-axis), and finally the k-index (negative of z-direction).

For establishing vertical and inclined faulting more accurately, it is advantageous to define the position of the grid cell by its corner point locations and displace them along the pillars that have been aligned with faults surfaces. Similarly, for modeling the erosion surfaces and pinch-outs of geological layers, the corner point format allows points to collapse along coordinate lines. The corner points can collapse along all four lines of a pillar so that a cell completely disappears in the presence of erosion surfaces. If the collapse is present in some pillars, the degenerate hexahedral cells may have less than six faces. This procedure creates non-matching geometries and non-neighboring connections in the underlying i-j-k topology (Lie, 2019). Fig. 2 illustrates the steps in the construction of the corner-point grids as explained above.

4.1. Two-point flux approximation in the corner-point grid geometry

In order to only highlight the calculation of the two-point flux approximation in the corner-point grid geometry and avoid complexities in presenting fully detailed governing equations, a simplified linear elliptic equation is used which serves as a model pressure equation for incompressible fluids, i.e.,

$$\nabla \cdot u = f, \tag{19}$$

where f is the source/sink term (wells), and u is the Darcy velocity, defined as

$$u = -\mathbf{K} \nabla p. \tag{20}$$

Finite volume discrete systems can be obtained by rewriting the equation in integral form, on discrete cell Ω_i, as

$$\int_{\partial \Omega_i} \vec{u} \cdot \vec{n} \, dS = -\int_{\Omega_i} q \, d\vec{x}. \tag{21}$$

The flux between the two neighboring cells i and k can be then written as

$$u_{i,k} = \int_{\Gamma_{i,k}} \vec{u} \cdot \vec{n} \, dS. \tag{22}$$

The faces $\Gamma_{i,k}$ are denominated half face as they are linked with a grid cell Ω_i and a normal vector $\vec{n}_{i,k}$. It is assumed that the grid matches with another one so that each interior half-face will have a twin half-face $\Gamma_{k,i}$ that has an identical area $A_{i,k} = A_{k,i}$ but an opposite normal vector $\vec{n}_{i,k} = -\vec{n}_{k,i}$. The integral over the cell face is approximated by the midpoint rule, and Darcy's law, i.e.,

$$u_{i,k} \approx A_{i,k} \left(\mathbf{K} \nabla p \right)(\vec{x}_{i,k}) \cdot \vec{n}_{i,k} \tag{23}$$
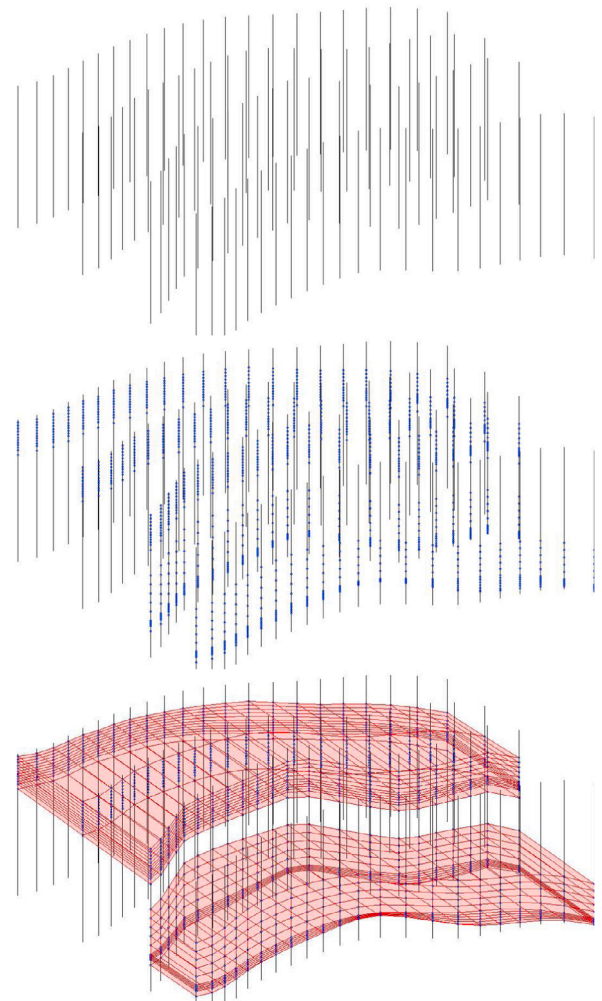

Fig. 2. Construction of a corner-point grid: Starting from the coordinate lines defining pillars (top), the corner-points are added to them (middle). A stack of cells is created for each set of four lines defining a pillar and at last the full grid is obtained (bottom).

where $\vec{x}_{i,k}$ indicates the centroid of $\Gamma_{i,k}$.

The one-sided finite difference is used to determine the pressure gradient as the difference between the pressure $\pi_{i,k}$ at the face centroid and the pressure at some point inside the cell. The reconstructed pressure value at the cell center is equal to the average pressure p_i inside the cell, thus,

$$u_{i,k} \approx A_{i,k} \mathbf{K_i} \frac{(p_i - \pi_{i,k}) \vec{c}_{k,i}}{|\vec{c}_{k,i}|^2} \cdot \vec{n}_{i,k} \Rightarrow u_{i,k} \approx T_{i,k}(p_i - \pi_{i,k}). \tag{24}$$

The vectors $\vec{c}_{k,i}$ are defined from cell centroids to face centroids. As shown in Fig. 3, face normals are assumed to have a length equal to the corresponding face areas $A_{i,k} \cdot \vec{n}_{i,k}$, i.e.,

$$T_{i,k} = A_{i,k} \mathbf{K_i} \frac{\vec{c}_{k,i} \cdot \vec{n}_{i,k}}{|\vec{c}_{k,i}|^2}. \tag{25}$$

The one-sided transmissibilities $T_{i,k}$ are related to a single cell and provide a two-point relation between the flux across a cell face and the pressure difference between the cell and face centroids. The proper name for these one-sided transmissibilities is half-transmissibilities as they are associated with a half-face (Karimi-Fard et al., 2004; Bosma et al., 2017).

Finally, the continuity of fluxes across all faces, $u_{i,k} = -u_{k,i}$, as well as the continuity of face pressures $\pi_{i,k} = \pi_{k,i} = \pi_{ik}$ are set. This leads to
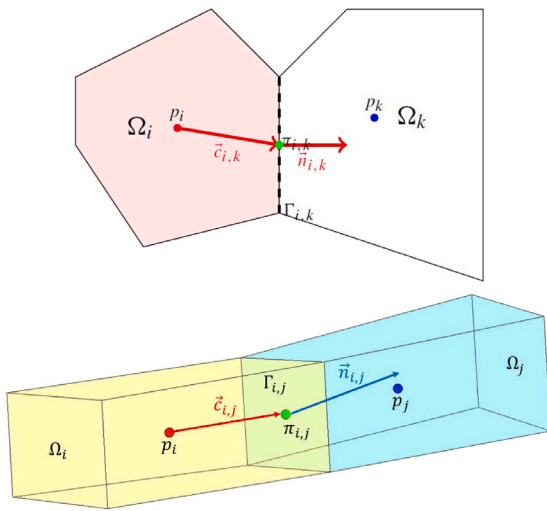
Fig. 3. Two cells used to define the two-point discretization on general 2D polygon cells (see the figure on top) and 3D polyhedral cells (see the figure at the bottom).

$$T_{i,k}^{-1} \, u_{ik} = p_i - \pi_{ik} \tag{26}$$

$$-T_{k,i}^{-1} \, u_{ik} = p_k - \pi_{ik}. \tag{27}$$

The interface pressure π_{ik} is then eliminated and the two-point flux approximation (TPFA) scheme is defined as

$$u_{ik} = \left[T_{i,k}^{-1} + T_{k,i}^{-1} \right]^{-1} (p_i - p_k) = T_{ik} \, (p_i - p_k). \tag{28}$$

T_{ik} is the transmissibility associated with the connection between the two cells. The TPFA scheme uses two "points", the cell averages p_i and p_k, to approximate the flux across the interface $\Gamma_{i,k}$ between cells Ω_i and Ω_k. The TPFA scheme in a compact form obtains a set of cell averages that meet the following system of equations

$$\sum_k T_{ik} \, (p_i - p_k) = q_i , \quad \forall \Omega_i \subset \Omega. \tag{29}$$

5. pEDFM for the corner-point grid geometry

In this section, pEDFM for the corner-point grid (CPG) geometry is described. Note that this development considers only convex hexahedral CPG geometries with planar faces. However, in some field-relevant geo-models, some interfaces may not be planar. For example, the model illustrated in Fig. 4 and the grid cells illustrated in Fig. 5 have some non-planar faces. To obtain the matrix–fracture intersections, in the presence of non-planar matrix grid interfaces, the pEDFM procedure approximates the non-planar interface with a planar interface. This approximation is explained further in this section. Note that the planar fractures can have any orientation in 3D with arbitrary crossing lines with other fractures.

As stated in the section for the discretization of the governing equations, sets of flux exchange terms are defined between the matrix and the explicit fractures. Inside each term, the connectivity index $(CI_{ij} = \frac{A_{ij}}{\langle d \rangle_{ij}})$ is considered. In the corner-point grid geometry, to calculate the area fraction (A_{ij}) of each overlapping fracture element inside the corresponding matrix grid cell, various geometrical functions are defined which can obtain the intersection between a quadrilateral (the 2D planar fracture grid cell in 3D geometry) and a hexahedron (the matrix grid cell in the corner-point grid geometry).

At first, the matrix grid cells that are overlapped by each element of each fracture need to be detected. To achieve this, the matrix cell with the shortest distance to the fracture element is detected. The
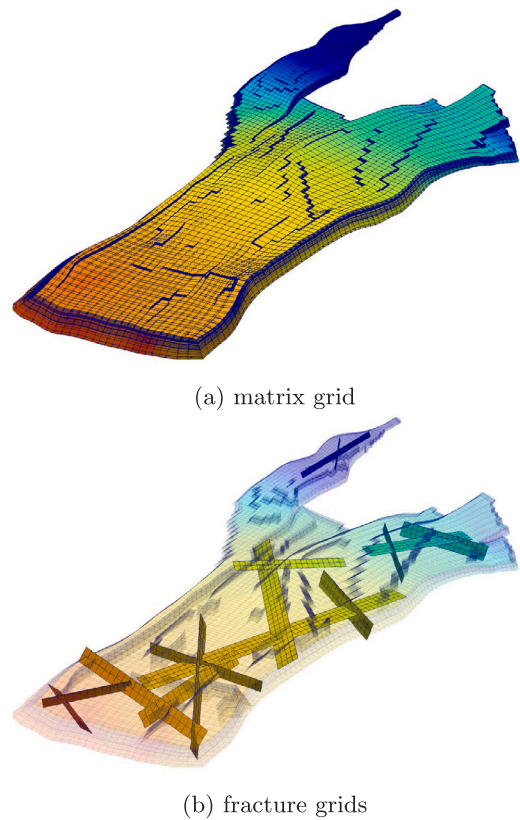

(a) matrix grid

(b) fracture grids

Fig. 4. An example of a fractured domain on the corner-point grid geometry. The domain presented in Fig. 4(a) is the well-known Norne oil-field which is a true representative of the real-field geometry (Lie, 2019). Fig. 4(b) is a realization of a fracture network inside the domain that was exclusively designed by the authors of this paper. Note that each sub-domain (matrix, and individual fractures) entail independent grid resolutions, and can have independent complexities (e.g. 3D orientation).

distance is calculated between the matrix cell center point and the corners of the fracture element. In a loop, it is checked whether the quadrilateral fracture element intersects with any of the quadrilateral faces of that hexahedral matrix cell. The fracture–matrix intersection points are then ordered counter-clockwise, and a polygon is formed from the intersection points. Various geometrical possibilities exist with regards to the intersection points and the polygons generated by them. More precisely, if only one or two intersection points are obtained, there is no polygon generated. As such, no area can be defined by the points, i.e., the intersection is a line or a single point (thus zero surface area). Alternatively, if between three to six intersection points are detected, one can form a polygon with them (either a triangle, a quadrilateral, a pentagon or a hexagon). The area of the polygon, i.e. A_{ij}, is then calculated by triangulation procedure. Once the area is calculated, the average distance between the fracture plate and the overlapped matrix grid cell, i.e. $\langle d \rangle_{ij}$, is computed. For this purpose, since complex geometries are considered, a numerical approach is developed. This numerical approach imposes a set of equidistant points within the hexahedral matrix grid cell. The distance of each point to the fracture plate is then calculated. Finally, the distances for all numerical points are then averaged and assigned to $\langle d \rangle_{ij}$ value. Having the area of the polygon and this average distance, the connectivity index is then calculated. Afterwards, using a flood-fill search algorithm (Newman, 1979), all the matrix grid cells that are overlapped by the mentioned fracture elements are detected and their connectivity indices are calculated. This procedure is done for each fracture element of each fracture plate. The flood-fill search algorithm ensures computational efficiency by avoiding unnecessary checks on the matrix grids that are not in the vicinity of the fracture element.
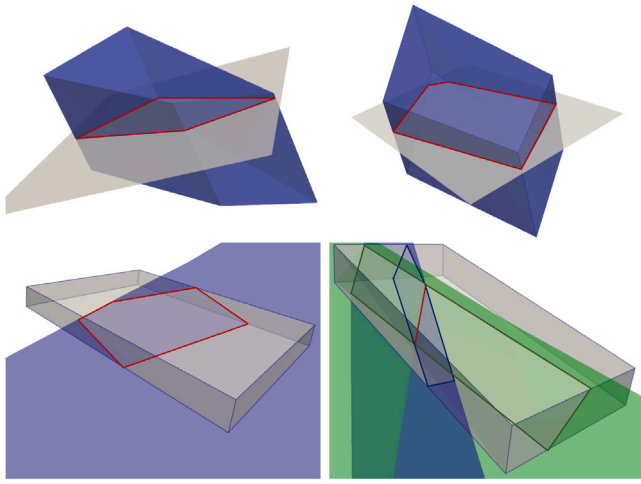
Fig. 5. The intersection between one or two fractures and a hexahedron in the corner-point grid geometry is illustrated in these images. Note that the intersections form irregular polygons. In the case of two fracture intersecting inside a matrix grid cell, i.e., image at the bottom right, the polygons formed by the overlap of the two fractures intersect on a line segment.

The algorithm above is performed on the computational CPG geo-model, assuming all matrix grid interfaces are planar. However, as mentioned before, field-relevant models could entail some non-planar interfaces. To employ our pEDFM-CPG in these scenarios, the developed algorithm applies approximate pEDFM connectivities for those non-planar interfaces. More precisely, prior to obtaining the intersection points between matrix and fracture elements, the non-planar interfaces are approximated into planar interfaces. To achieve this, the middle point of the non-planar interface is acquired via arithmetic averaging of the coordination of the four corners. This middle point together with the normal vector of the corresponding interface are used to formulate the equation of a planar quadrilateral that best fits this interface. This planar interface is then used to detect and realize the intersection points within the pEDFM algorithm. It is also worth mentioning that the approximation of non-planar interfaces into planar quadrilateral plane segments results in slight (in many cases negligible) volume shifts of the hexahedral grid cells between neighboring cells of the interface. Note that as any volume shift in one grid cell is followed by identical volume shift with opposite sign in the other neighboring grid cell, hence, this approximation remains strictly mass conservative. Moreover, such approximation is primarily local, for each non-planar interface, and as such remains much smaller than the fine-scale grid cell size in each direction. However, it allows for the major flexibility of having the developed pEDFM also applicable to non-planar matrix interfaces.

The first step in the development of the pEDFM for the corner-point grid geometry is to flag all the interfaces between the matrix cells that a fracture plate interrupts the connection between their cell centers. To detect the affected interfaces, first, the list of all the matrix grid cells that are overlapped by a fracture element is considered. In a loop, for each overlapped matrix grid cell, a line segment that connects the cell center of the mentioned matrix grid cell and the cell center of each of its neighboring cells is defined. If the fracture plate intersects the line segment, the interface between the two neighboring matrix grid cells is affected by the crossing fracture. Therefore a projection of the fracture element is obtained on the affected interface. In Fig. 6, the fracture element f is assumed to overlap with the matrix grid cell Ω_i with an area fraction of A_{if}. A set of projections is defined on the interfaces between the overlapped matrix grid cell Ω_i and its neighboring grid cells that are affected by the crossing (i.e., Ω_j and Ω_k). For the interface

between grid cells Ω_i and Ω_j (denoted as $\Gamma_{i,j}$) the projection area fraction $A_{if \perp \Gamma_{i,j}}$ is obtained via

$$A_{if \perp \Gamma_{i,j}} = A_{if} \times \cos(\gamma). \tag{30}$$

Here, γ is the angle between the fracture element f and the interface $\Gamma_{i,j}$ connecting the matrix grid cell Ω_i and the neighboring grid cell (in this example, Ω_j). On the zoomed-in section of Fig. 6, this projection area fraction is highlighted in red. Similarly, the projection area fractions on the interfaces between all the neighboring matrix grid cells that are intersected by fracture elements are calculated based on the same formulation. Thereafter, a continuous projection path (shown in Fig. 6 as solid lines in light-blue color) is obtained on the interfaces. This projection path, disconnects the connections between the neighboring cells on both sides of this path, thus allowing a non-parallel and consistent flux exchange (i.e., through matrix–fracture–matrix).

After obtaining the projection areas, a set of new transmissibilities are defined to provide connection between the fracture element f and each non-neighboring matrix grid cell (i.e., j and k in the example shown in figure. 6):

$$T_{i_e f} = \frac{A_{if \perp \Gamma_{i,j}}}{\langle d \rangle_{i_e f}} \lambda_{i_e f}, \tag{31}$$

with $\langle d \rangle_{i_e f}$ defined as the average distance between the fracture element f and matrix grid cell i_e, and $\lambda_{i_e f}$ being the effective fluid mobility between these two cells. Therefore, the transmissibility between the matrix grid cell i and its corresponding neighboring cells is re-adjusted as

$$T_{ii_e} = \frac{A_{ii_e} - A_{if \perp \Gamma_{i,j}}}{\Delta x_e} \lambda_{i_e f}. \tag{32}$$

These transmissibilities are modified via multiplication of a factor denoted as α and defined as a fraction of the projection area divided by the total area of that interface as the following:

$$\alpha = \frac{A_{if \perp \Gamma_{i,j}}}{A_{ii_e}}. \tag{33}$$

As an example, if half of an interface area between two cells is covered by the projection of a fracture cell, the alpha factor for that interface will be $\alpha = 0.5$. The transmissibilities are modified via

$$T_{ii_e} := T_{ii_e} \times (1 - \alpha). \tag{34}$$

One should consider that due to the continuation of a fracture plate, for all the overlapping fracture elements (except for the boundaries of the fractures), the projections will cover the entire area of the affected interfaces. This means that α is 1.0 for most of the cases. Therefore, to simplify the implementation, all the non-zero α factors are modified to be 1.0 forcing full projections from the boundaries of the fractures on the affected interfaces.

Algorithm 1 describes the pEDFM procedure for the corner-point grid geometry, where the steps explained above are pointed step-by-step.

6. Simulation results

Numerical results of various test cases are presented in this section. The first two test cases compare the pEDFM model on the Cartesian grid geometry with the pEDFM on the corner-point grid geometry. The third test case demonstrates the pEDFM result on a non-orthogonal grid model. Thereafter, we move towards a series of geologically relevant fields. Using the pEDFM on the corner-point grid geometry, a number of synthetic (highly conductive) fractures and (impermeable) flow barriers are added to the geologically relevant models. The computational performance of this method will not be benchmarked as the purpose of these simulation results is to demonstrate the pEDFM on the corner-point grid geometry as a proof-of-concept.

Tables 1 and 2 show the mutual input parameters that are used for the test cases with the isothermal multiphase and the geothermal single-phase flow models respectively.
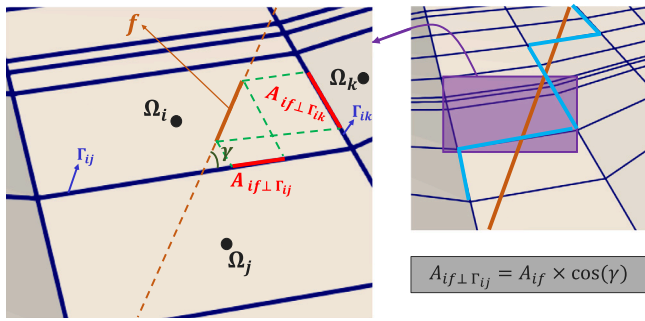
Fig. 6. pEDFM Illustration for a rock matrix in the corner-point grid geometry and an overlapping fracture. Due to pEDFM modifications, new non-neighboring connections between the fracture elements and the non-overlapped matrix cells are defined. The matrix–matrix connectivities are modified only if the fracture plate interrupts the line-segment that passes through the cell centers of each two neighboring matrix grid cells. (For interpretation of the references to color in this figure legend, the reader is referred to the web version of this article.)

Table 1
Input parameters of the fluid and rock properties for the isothermal multiphase flow.

Property	Value
Matrix porosity (ϕ)	0.2 [–]
Fractures permeability (min)	10^{-22} [m^2]
Fractures permeability (max)	10^{-6} [m^2]
Fractures aperture	5×10^{-3} [m]
Fluid viscosity (phase 1, μ_1)	0.001 [Pa s]
Fluid viscosity (phase 2, μ_2)	0.003 [Pa s]
Fluid density (phase 1, ρ_1)	1000 [kg/m^3]
Fluid density (phase 2, ρ_2)	850 [kg/m^3]
Initial pressure of the reservoir	2×10^7 [Pa]
Initial saturation (phase 1, S_1)	0.0[–]
Initial saturation (phase 1, S_2)	1.0[–]
Injection Pressure	5×10^7 [Pa]
Production Pressure	1×10^7 [Pa]

Table 2
Input parameters of the fluid and rock properties for the geothermal single-phase flow used in some test cases.

Property	Value
Rock thermal conductivity (Λ_r)	4 [W/m K]
Fluid thermal conductivity (Λ_f)	0.591 [W/m K]
Rock density (ρ_r)	2750 [kg/m^3]
Fluid specific heat (C_{p_f})	4200 [J/kg K]
Rock specific heat (C_{p_r})	790 [J/kg K]
Matrix porosity (ϕ)	0.2[–]
Fractures permeability (min)	10^{-20} [m^2]
Fractures permeability (max)	10^{-8} [m^2]
Fractures aperture	5×10^{-3} [m]
Initial pressure of the reservoir	1.5×10^7 [Pa]
Initial temperature of the reservoir	400 [K]
Injection Pressure	2×10^7 [Pa]
Injection Temperature	300 [K]
Production Pressure	1×10^7 [Pa]

6.1. Test case 1: 2D heterogeneous fractured reservoir (square)

In this test case, the pEDFM on the Cartesian grid is compared with the corner-point grid geometry. For this reason, a box-shaped hetero-geneous $100\,[\text{m}] \times 100\,[\text{m}]$ domain containing 30 fractures with mixed conductivities is considered. The length of each fracture is different but the size of their aperture is identical and set to $a_f = 5 \cdot 10^{-3}$ [m]. A 136×136 grid is imposed on the rock matrix and the fracture network consists of 1024 grid cells (in total 19520 cells). The permeability of the matrix ranges from $K_{m_{min}} = 1.2 \times 10^{-15}$ [m^2] to $K_{m_{max}} = 1.2 \times 10^{-12}$ [m^2], and the permeability of the fracture network has the range of $K_{f_{min}} = 10^{-22}$ [m^2] and $K_{f_{max}} = 10^{-6}$ [m^2]. Two injection wells are located at the bottom left and top left corners with an injection pressure of $p_{\text{inj}} =$

Algorithm 1 The pEDFM algorithm for the corner-point grid geometry.

Read the corner-point grid data of the domain.
Scan the input file including the fractures geometry.
Discretize the fractures and generate the grids.
Obtain the EDFM connectivities:
for $f = 1$ *to* Num_{frac} **do**
  for $i_f = 1$ *to* $Num_{grid}(f)$ **do**
    Find the closest matrix grid cell (Im)
    for $j = 1$ *to* Num_{faces} **do**
      Obtain the intersections between the fracture element and all the faces
    end
    Order the intersection points counter-clockwise.
    if $Num_{intersection\ points} > 2$ **then**
      Calculate the area of the intersection polygon $A_{ij}^{m,f}$.
      Populate the matrix grid cell Im with equidistant points.
      Calculate the average distance between the fracture plate and the matrix grid cell $\langle d \rangle_{ij}$.
      Calculate the connectivity index CI^{m,f_i}.
    end
    Add the neighbors of the matrix grid cell Im to the checklist.
    for $n = 1$ *to* $Num_{neighbors}$ **do**
      Obtain the intersections.
      if $Num_{intersection\ points} > 2$ **then**
        Repeat the procedure and add the neighbors of this grid cell to the checklist.
      end
    end
  end
end
Obtain the pEDFM projections:
for $f = 1$ *to* Num_{frac} **do**
  for $i_f = 1$ *to* $Num_{grid}(f)$ **do**
    for $Im = 1$ *to* $Num_{EDFM\ connections}$) **do**
      Define a linesegment connecting the cell center of matrix grid cell Im to its neighbor.
      if *fracture* f *intersects the line segment* **then**
        Obtain the projection area.
        Calculate the α factor.
        Compute the average distance to the neighbor of the grid cell Im.
        Compute the connectivity index for the neighbor of the grid cell Im.
      end
    end
  end
end

2×10^7 [Pa]. Additionally, there are two production wells at the bottom right and the top right corners with a pressure of $p_{\text{prod}} = 1 \times 10^7$ [Pa]. Table 2 demonstrates the input parameters of this test case. Fig. 7 shows the results of the simulation using both Cartesian Grid and corner-point geometry.

Note that in this test case (and the test case 2), the x, y, z coordinates of the grids of the Cartesian geometry and the corner-point grid geometry are identical. However, the grids are generated with different geometrical approaches. In one scenario, the grid cells are discretized using the Cartesian grid geometry and the grid cells are indexed in every of the x, y, z directions ($i \in \{1, \dots, N_x\}$, $j \in \{1, \dots, N_y\}$, $k \in \{1, \dots, N_z\}$). For this scenario the pEDFM for the Cartesian grid is used which has already been developed (Tene et al., 2017). In the other scenario, the grid cells are generated using the corner-point grid geometry where a list of nodes and a list of all the interfaces and transmissibilities are generated. the pEDFM for the corner-point grid
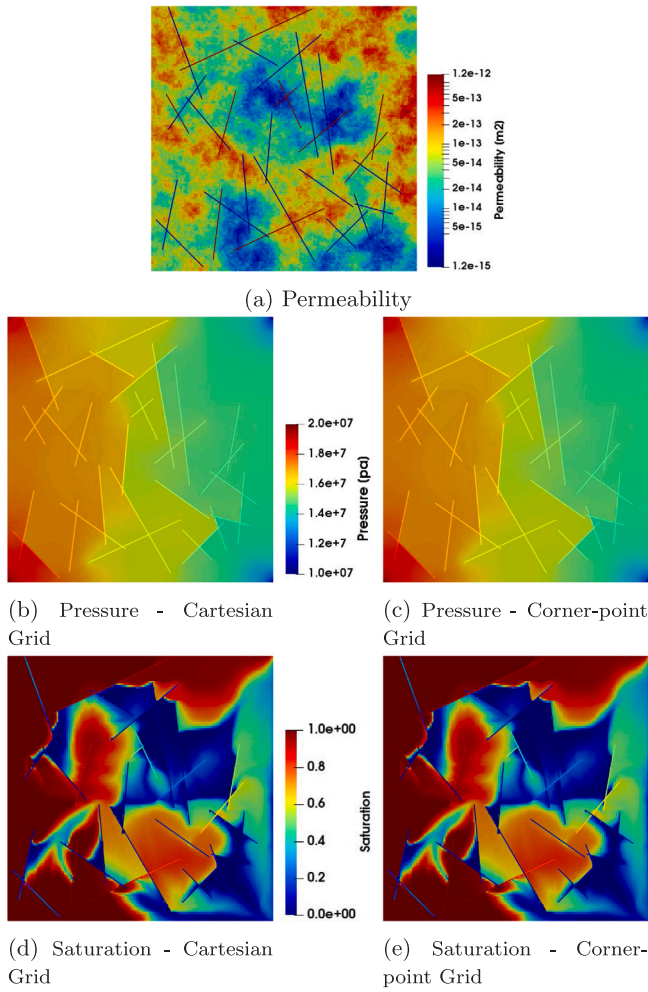
(a) Permeability

(b) Pressure - Cartesian Grid

(c) Pressure - Corner-point Grid

(d) Saturation - Cartesian Grid

(e) Saturation - Corner-point Grid

Fig. 7. Test case 1: 2D Heterogeneous. Fig. 7(a) illustrates the permeability map of the system. The Figs. 7(b) and 7(c) show the pressure solutions at a specific time-step for the Cartesian grid and the corner-point grid geometry respectively. The figures on the bottom row 7(d) and 7(e) visualize the saturation distribution at the same time-step.

geometry that is developed in this work is used for this scenario. Therefore, the size and positioning of the grid cells in the two scenarios are identical, though have been generated with different geometrical approaches.

The results of the both scenarios show a match visually. In order to quantify the difference between the results of the two different geometrical approach for the pEDFM, a average relative error (in second norm) is calculated for the pressure and the saturation distributions over the entire simulation time. This relative error for each variable x is calculated as

$$e_x = \frac{\| x_{\text{Cart}} - x_{\text{CPG}} \|_2}{\| x_{\text{Cart}} \|_2}, \tag{35}$$

where x is a solution vector (of either of the main unknowns) and the subscripts Cart and CPG indicate Cartesian grid and the corner-point grid geometry. The errors calculated for this test case are $e_p = 1.55 \times 10^{-5}$ and $e_S = 1.60 \times 10^{-4}$.

6.2. Test case 2: 3D homogeneous fractured reservoir (box)

These test cases, similar to the test case 1, show a comparison for the pEDFM on the Cartesian grid versus the corner-point grid geometry. A 3D $100\,[\text{m}] \times 100\,[\text{m}] \times 40\,[\text{m}]$ domain containing 15 lower dimensional fractures with different geometrical properties is considered. A
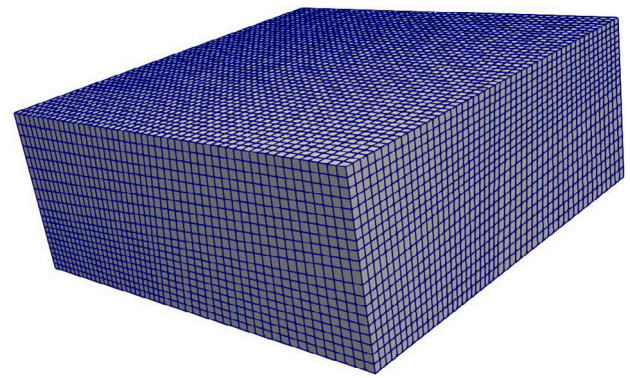

Fig. 8. Test case 2: The non-orthogonal mesh structure used in this test case. The domain is a 3D Cartesian box, but the grids have tilted pillars in two of the dimensions, creating non-orthogonal grids.
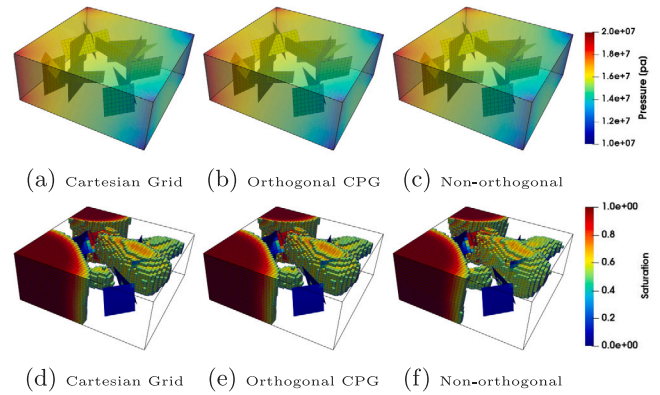

(a) Cartesian Grid (b) Orthogonal CPG (c) Non-orthogonal

(d) Cartesian Grid (e) Orthogonal CPG (f) Non-orthogonal

Fig. 9. Test case 2: 3D Homogeneous box. The figures in the upper row show the pressure solutions at a specific time-step for the Cartesian grid and the CPG geometries respectively. The figures on the bottom row illustrate the saturation solutions at the same time-step.

$50 \times 50 \times 20$ grid is imposed on a rock matrix. The fracture network contains 1005 grid cells (total of 51005 grid cells). The rock matrix has a permeability of $K_m = 10^{-14}\,[\text{m}^2]$. The fracture network consists of both highly conductive fractures with a permeability of $K_f = 10^{-6}\,[\text{m}^2]$ and flow barriers with a permeability of $K_f = 10^{-22}\,[\text{m}^2]$. Two injection wells exist on the bottom left and top left boundaries with a pressure of $p_{\text{inj}} = 2 \times 10^7\,[\text{Pa}]$. Similarly, two production wells are located at the bottom right and top right boundaries with a pressure of $p_{\text{prod}} = 1 \times 10^7\,[\text{Pa}]$. All wells are vertical and perforate the entire thickness of the reservoir. Two different grids are considered using the CPG geometry: one with orthogonal grids where the coordinates of all the grid cells are identical with those in the Cartesian grid geometry, and one with non-orthogonal grids where the pillars of the grids are slightly tilted. To provide a better insight, the non-orthogonal grid mesh is shown in Fig. 8. As shown, the domain remains a Cartesian box, but the CPG grid is tilted to verify its consistency.

Fig. 9 illustrates the simulation results for he Cartesian Grid, and the two sets of CPG models.

Fig. 10 shows the errors between the results of the Cartesian grid geometry (as the reference solution) and the two CPG cases (orthogonal and non-orthogonal). Similar to the previous test case, a match is visible between the results of the Cartesian grid and the orthogonal corner-point grid, with errors (calculated via Eq. (35)) of $e_p = 1.71 \times 10^{-9}$ and $e_S = 2.47 \times 10^{-8}$. The difference between the solutions of the Cartesian grid and the non-orthogonal corner-point grids are greater as the different grid geometry results in different connectivities ($e_p = 1.03 \times 10^{-2}$ and $e_S = 4.44 \times 10^{-2}$).
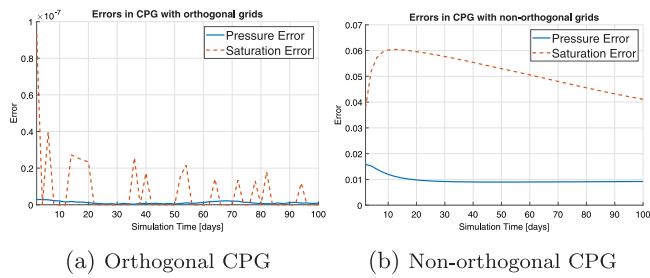
(a) Orthogonal CPG

(b) Non-orthogonal CPG

Fig. 10. Test case 2: The errors (calculated via Eq. (35)) of the pressure and saturation results between the Cartesian grid geometry (as the reference solution) and the CPG geometries: one with orthogonal grids (Fig. 10(a)) and one with non-orthogonal grids (Fig. 10(b)).

### 6.3. Test case 3: 3D reservoir with non-orthogonal grids

The third test case (Fig. 11) demonstrates the capability of the pEDFM method on the reservoir model based on corner point grids. The grid cells in test case 2 were deformed to create a distorted version of that model. The model allows for the testing of the pEDFM implementation in a non-orthogonal grid system. The same dimensions and gridding from test case 2 are used in this test case. The fracture network consisting of 15 fractures is discretized in 876 grids, and a total of 50876 grid cells are imposed on the entire domain.

Two different scenarios are considered in this test case. In the first scenario some fractures are considered as highly conductive while the others are given a very low permeability and are considered to be flow barriers (shown in Fig. 11(a) with yellow color for high permeability and blue color for low permeability). In the second scenario, the permeability of the fractures is chosen as the inverse of scenario 1 11(b), i.e., the low conductive fractures are now highly conductive and vice versa. The values of permeability for the matrix and (low and high conductive) fractures are identical to the ones in test case 2. The well pattern and pressure restrictions are also the same as in the previous test case.

The pressure and saturation results of scenario 1 are shown in Figs. 12(a) and 12(c) respectively (at the left side of Fig. 12). As the grid geometry and the gridding system of this test case are not similar to the previous test case, it is not possible to compare the two test cases. The pressure and saturation distribution of the second scenario (at the same simulation time) can be observed at right side of Fig. 12.

In the first scenario, the flow barriers are close to the injection wells, thus restricting the displacement of the injecting phase towards the center of the domain (Fig. 12(c)). Therefore, a high pressure gradient is visible near the injection wells (Fig. 12(a)) as the low permeability fractures limit the flux through the domain. In the second scenario, the highly conductive fractures are near the injection wells, and the saturation profile increases through the whole thickness of the domain (Fig. 12(d)). The pressure profile is uniformly distributed in the reservoir as there is no flux restriction near the wells (Fig. 12(b)).

Additionally, to perform a grid resolution sensitivity analysis of the developed model, this test case was used with three different grid resolutions. While keeping all the input parameters identical as the ones that were mentioned above, three different computational grids (using corner-point grid geometry) were imposed on this domain, namely, $80 \times 80 \times 32$, $40 \times 40 \times 16$ and $20 \times 20 \times 8$ for the rock matrix, and 2852, 757 and 173 for the fracture network, respectively. Fig. 13 shows the saturation distribution of these three different gird resolutions at a simulation time of $t = 100 [days]$. The results of the two lower grid resolutions (i.e., $20 \times 20 \times 8$ and $40 \times 40 \times 16$) were compared against the results of the highest grid resolution (i.e., $80 \times 80 \times 32$), meaning that the results of the $80 \times 80 \times 32$ grid resolution is used as reference in the calculation of the error. The relative error for pressure
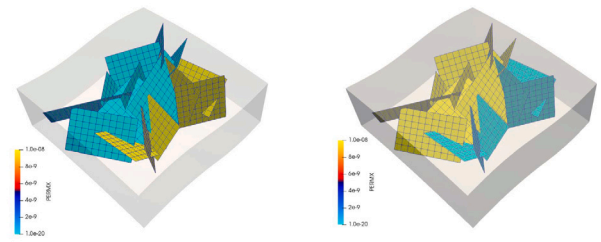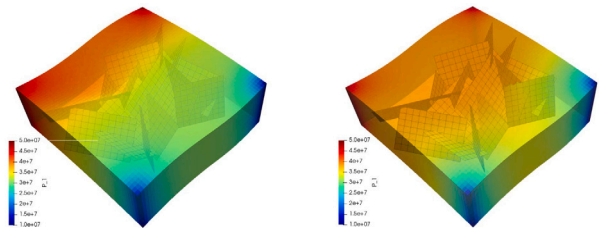

(a) Fractures permeability (scenario 1)

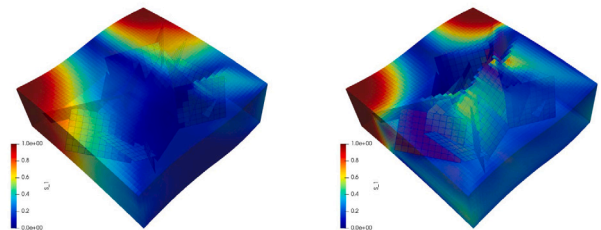(b) Fractures permeability (scenario 2)
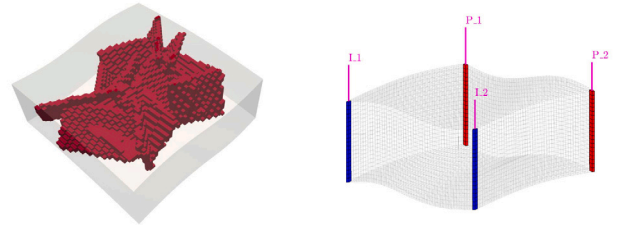
(c) Matrix cells overlapped by fractures

(d) The well geometry

Fig. 11. Test case 3: A 3D fractured deformed box with non-orthogonal grid in the corner-point grid geometry. The Figs. 11(a) and 11(b) on top show the permeability of the fractures for the scenarios 1 and 2 respectively. The Fig. 11(c) on the bottom left illustrates the matrix grid cells that are overlapped by the fractures. Fig. 11(d) on the bottom right shows the geometry of injection and production wells.

(a) Pressure (scenario 1)

(b) Pressure (scenario 2)

(c) Saturation (scenario 1)

(d) Saturation (scenario 2)

Fig. 12. Test case 3: A 3D fractured deformed box with a non-orthogonal grid in the corner-point grid geometry. The Figs. 11(a) and 11(b) on top show the permeability of the fractures for the scenarios 1 and 2 respectively. The Fig. 11(c) on the bottom left illustrates the matrix grid cells that are overlapped by the fractures. Fig. 11(d) on the bottom right shows the geometry of injection and production wells.

and saturation results are given in Fig. 14. These errors are calculated as:

$$e_x = \frac{\| x_{\text{HighRes}} - x_{\text{LowRes}} \|_2}{\| x_{\text{HighRes}} \|_2}, \qquad x = \{P, S_w\} \tag{36}$$

(a) $20 \times 20 \times 8$ (b) $40 \times 40 \times 16$ (c) $80 \times 80 \times 32$
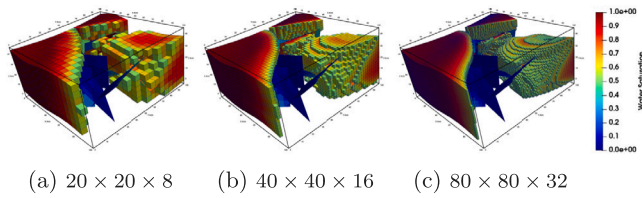
Fig. 13. Test case 3: Grid resolution sensitivity analysis with three different grid resolutions (with non-orthogonal corner-point grids) imposed on the computational domain. The figures show the saturation distribution at $t = 100[days]$ of simulation time. Only the grid cells with the saturation values of higher than $S_w = 0.5$ are visible.
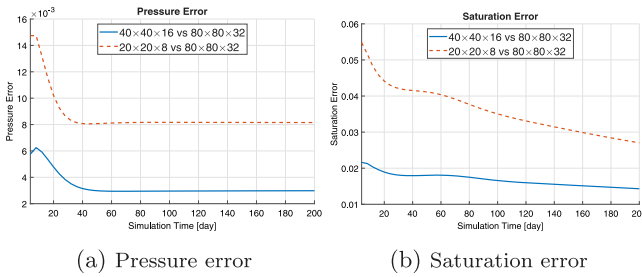

(a) Pressure error   (b) Saturation error

Fig. 14. Test case 3: Grid resolution sensitivity analysis with three different grid resolutions (with non-orthogonal corner-point grids) imposed on the computational domain. These figures illustrate the pressure and saturation errors of the results from different grid resolutions.
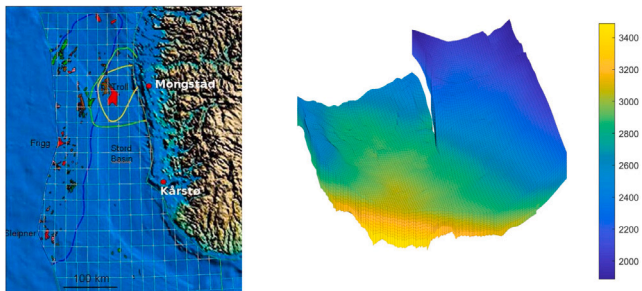

Fig. 15. Test case 4: The location of the Johansen formation can be observed on the left figure. This formation is located within the green curve in the map, and the yellow curve represents areas where seismic data have been acquired (courtesy of Gassnova). The figure on the right shows the depth map of the Johansen model (NPD5 data set).

6.4. Test case 4: The Johansen formation

The water-bearing Johansen formation was a potential candidate for CO_2 storage in a project promoted by the Norwegian government. The Norwegian continental margin has excellent potential for CO_2 storage options in saline aquifers.

The Johansen formation (Eigestad et al., 2009) is located in the deeper part of the Sognefjord delta, offshore Mongstad on Norway's southwestern coast (see Fig. 15). It belongs to the Lower Jurassic Dunlin group and is interpreted as a laterally extensive sandstone, and it is overlaid by the Dunlin shale and below by the Amundsen shale. A saline aquifer exists in the depth levels ranging from 2200[m] to 3100[m] below the sea level. The depth range makes the formation ideal for CO_2 storage due to the pressure regimes existent in the field (providing a thermodynamical situation where CO_2 is in its supercritical phase).

These formations have uniquely different permeabilities and perform very different roles in the CO_2 sequestration process. The Johansen sandstone has relatively high porosity and permeability, and it is suitable to store CO_2. The low-permeability overlaying Dunlin shale acts as a seal that avoids the CO_2 from leaking to the sea bottom layers.
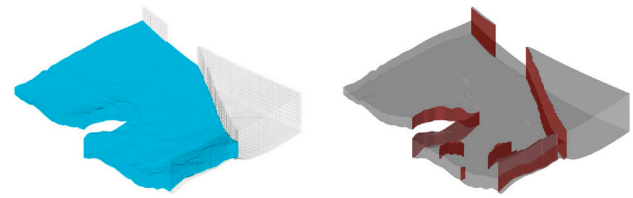

Fig. 16. Test Case 4: Illustration of the Johansen model (NPD5 data set). The left figure represents the active section of the model or NPD5, highlighted with blue color, and the right figure shows the faults marked with red color. (For interpretation of the references to color in this figure legend, the reader is referred to the web version of this article.)

The Johansen formation has an average thickness of nearly 100[m], and the water-bearing region extends laterally up to 60[km] in the east–west direction and 100[km] in the north–south direction. The aquifer has good sand quality with average porosities of roughly 25%. This implies that the Johansen formation's theoretical storage capacity can exceed one Gigaton of CO_2 providing the assumption of residual brine saturation of about 20%. The northwestern parts of the Johansen formation are located some 500[m] below the operating Troll field, one of the North Sea's largest hydrocarbon fields.

6.4.1. Data set

The MatMoRA project has created five models of the Johansen formation: one full-field model ($149 \times 189 \times 16$ grids), three homogeneous sector models ($100 \times 100 \times n$ for $n = 11, 16, 21$), and one heterogeneous sector model ($100 \times 100 \times 11$) also known as the NPD5 sector (Eigestad et al., 2009). In this work, the last data set (NPD5) has been used. The NPD5 sector can be seen in Fig. 16. In the left side of this figure, the NPD5 sector is highlighted with blue color.

In the discretized computational grids, the Johansen formation is represented by five layers of grid cells. The Amundsen shale below the Johansen formation and the low-permeable Dunlin shale above are characterized by one and five cell layers, respectively. The Johansen formation consists of approximately 80% sandstone and 20% claystone, whereas the Amundsen formation consists of siltstones and shales, and the Dunlin group has high clay and silt content.

6.4.2. Rock properties

The Johansen sandstone is a structure with a wedge shape pinched out in the front part of the model and divided into two sections at the back. Fig. 17 shows two different selections, i.e., the entire formation (Figs. 17(a) and 17(c)) and the NPD5 sector of the formation (Figs. 17(b) and 17(d)).

The porosity map of the entire model is visible in Fig. 17(a), and Fig. 17(b) shows the cells with porosity values larger than 0.1 that belong to Johansen formation. Similarly, the permeability map of the entire formation is shown in Figs. 17(c), and Fig. 17(d) illustrates the permeability of the NPD5 sector where the Dunlin shale above the Johansen and the Amundsen shale below the Johansen formation are excluded. The permeability tensor is diagonal, with the vertical permeability equivalent to one-tenth of the horizontal permeability. In both graphs, the permeability is represented by a logarithmic color scale.

6.4.3. Simulation results

The "NPD5" sector of the Johansen formation model (Lie, 2019) is used in the following test case. It is a corner-point grid reservoir model that consists of $100 \times 100 \times 11$ grid cells from which 88775 grid cells are active. The rock properties of the Johansen formation available as public data were given as input in the simulation. A network of 121 fractures is embedded in the reservoir geological data set that contains both highly conductive fractures and flow barriers with permeability of $K_{f_{max}} = 10^{-8}$ [m^2] and $K_{f_{min}} = 10^{-20}$ [m^2] respectively. The model is

(a) Porosity of the entire formation

(b) Porosity of the NPD5 sector

(c) Permeability of the entire formation
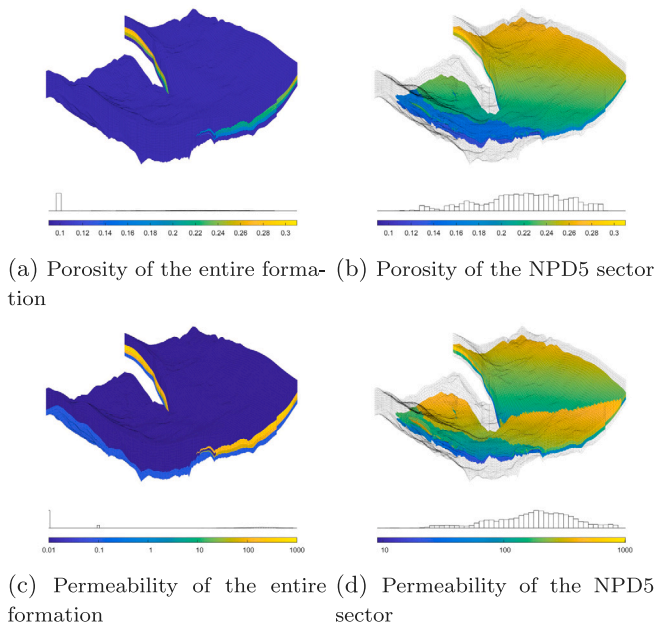
(d) Permeability of the NPD5 sector

Fig. 17. Test Case 4: Porosity and permeability of the entire Johansen formation and the NPD5 sector). The left figures show porosity and permeability of the whole model, whereas the right figures show the porosity and permeability of the NPD5 sector (sandstone).

Fig. 18. Test case 4: The Johansen formation. The histogram shows the range of the number of neighboring connections between the grid cells. The vertical axis displays the number of counts for a specific number of neighbors for a cell in logarithmic scale.

(a) Fractures permeability (scenario 1)

(b) Fractures permeability (scenario 2)

(c) Matrix cells overlapped by fractures

(d) Location of injection and production wells

Fig. 19. Test case 4: The Johansen formation with 9 wells and a set of 150 synthetic fractures (with mixed conductivities). The figures on top show the fracture networks with different permeabilities for scenario 1 (top left) and scenario 2 (top right). The figure at bottom left illustrates the highlighted matrix cells that are overlapped by the fractures network. And the figure at bottom right shows the schematics of the injection and production wells.

bounded by two shale formations. Therefore the fractures were placed inside the Johansen formation (layers 6 to 10). In total 150 fractures are embedded in the model, and the fracture network consists of 3494 grid cells (in total 92269 grid cells for matrix and fractures). Five injection wells with pressure of $p_{inj} = 5 \times 10^7$ [Pa] and four production wells with pressure of $p_{inj} = 1 \times 10^7$ [Pa] were placed in the model. Wells are vertical and drilled through the entire thickness of the model. Fig. 19(d) illustrates the location of the injection and production wells in this test case. Moreover, Fig. 18 shows a histogram of the number of the neighboring connections between the matrix grid cells of this field. While the majority of the grid cells have 5 or 6 neighbors, there are grid cells that have more than 6 neighbors due to non-matching grid topology.

In the "NPD5" computational model of the Johansen formation, 29 percent of the interfaces are non-planar. Approximating these interfaces with planar quadrilateral interfaces results in 1.57 percent of volume shift in each grid cell by average. However, as mentioned previously, mass conservation is guaranteed and no inconsistency is generated.

Two scenarios are considered with two different fracture networks of mixed conductivities. While the geometries of both fracture networks are identical, the permeability values of the fractures from scenario 1 are inverted for the scenario 2. This implies that the highly conductive fractures in the fractures network of scenario 1 act as flow barriers in the 2nd scenario and the flow barriers of scenario 1 are modified to be highly conductive fractures in the scenario 2. Figs. 19(a) and 19(b) display the fractures networks of scenario 1 and scenario 2 respectively. The matrix grid cells overlapped by the fractures are visible in Fig. 19(c) (see Fig. 19).

The simulation results of the first scenario are shown in Figs. 20 and 21. The injection wells are surrounded by highly conductive fractures that facilitate the flow since the model's dimensions are considerably large (approximately 50[km]×50[km]). The pressure distribution in the reservoir is shown in Fig. 20. High pressure values are observed in a large section of the reservoir as there is no restriction for flow from the wells, and two shale formations bound the Johansen sandstone. One can interpret that the high pressure drops observed in some regions are caused by presence of low permeable fractures (or flow barriers)
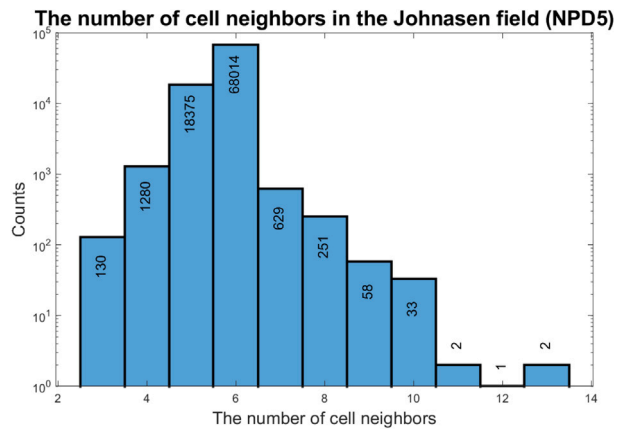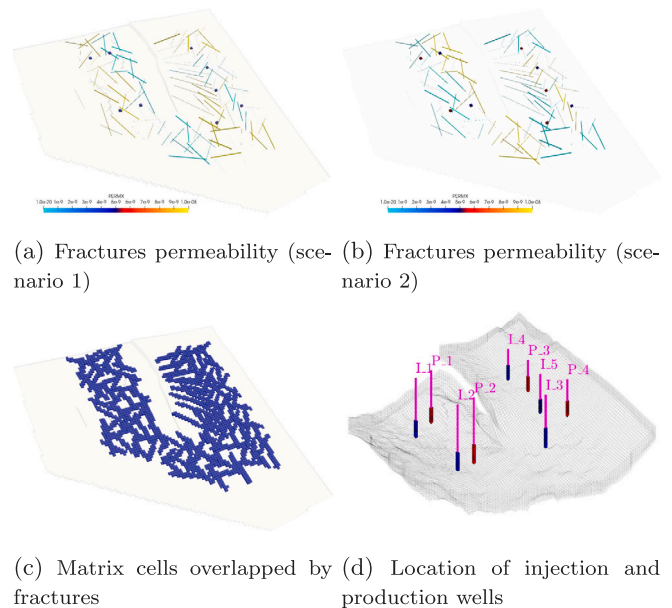
in those regions. The saturation displacement is considerably enhanced by the highly conductive fractures (Fig. 21) located near the injection wells.

For the second scenario, the results are presented in Figs. 22 and 23. The injection wells are surrounded by low conductive fractures which restrict the flow from the injection wells towards the production wells. The pressure distribution differs considerably when compared to the first scenario. The flow barriers near the wells result in high pressure drops in the vicinity of the injection wells. The saturation displacement (Fig. 23) is lower than that of scenario 1 due to presence of low conductive fractures near the injection wells.

6.5. Test case 5: The Brugge model

The Brugge model is an SPE benchmark study conceived as a reference platform to assess different closed-loop reservoir management
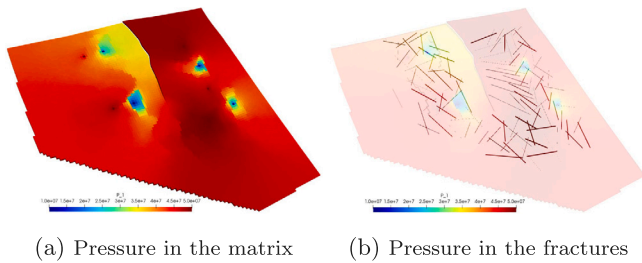
(a) Pressure in the matrix   (b) Pressure in the fractures

Fig. 20. Test case 4: The pressure profile of the Johansen formation for the simulation scenario 1. The figure on the left illustrates the pressure distribution in the matrix grid cells. The transparency of this figure is increased to make the fractures visible and to display the pressure profile in the fractures in the figure on the right.
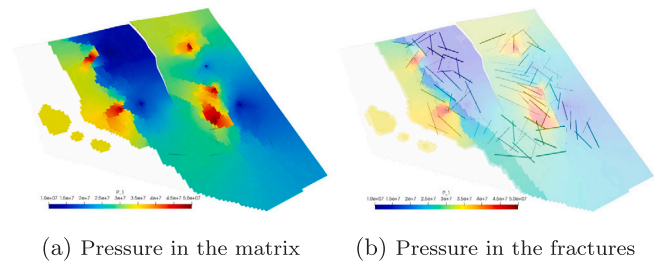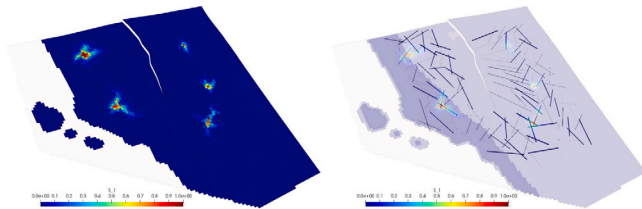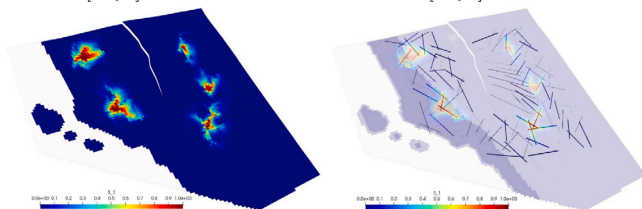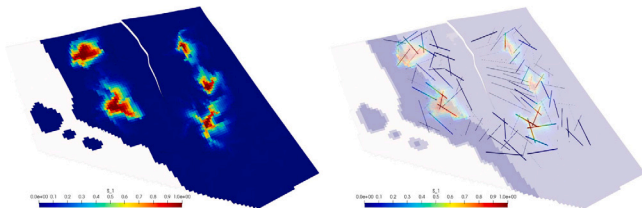

(a) Pressure in the matrix   (b) Pressure in the fractures

Fig. 22. Test case 4: The pressure profile of the Johansen formation for the simulation scenario 2. The figure on the left illustrates the pressure distribution in the matrix grid cells. To make the pressure profile of the fractures visible, the transparency of the left side figure is increased and it is presented in the right side figure.

(a) Saturation in the matrix after 5000[days]   (b) Saturation in the fractures after 5000[days]

(c) Saturation in the matrix after 20000[days]   (d) Saturation in the fractures after 20000[days]
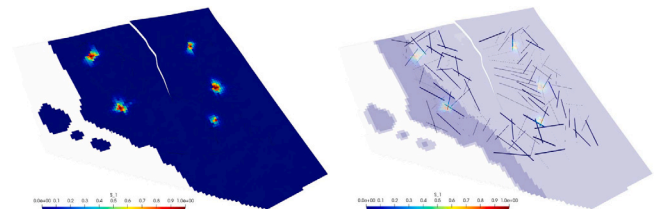
(e) Saturation in the matrix after 35000[days]   (f) Saturation in the fractures after 35000[days]

Fig. 21. Test case 4: The saturation profile of the Johansen formation for the simulation scenario 1. The figures on the left illustrate the saturation profile in the matrix grid cells and the figures on the right side show the saturation maps in the fractures. From the top row towards the bottom row, the saturation profiles are displayed for simulations times 5000, 20000 and 35000[days] respectively.

(a) Saturation in the matrix after 5000[days]   (b) Saturation in the fractures after 5000[days]

(c) Saturation in the matrix after 20000[days]   (d) Saturation in the fractures after 20000[days]

(e) Saturation in the matrix after 35000[days]   (f) Saturation in the fractures after 35000[days]

Fig. 23. Test case 4: The saturation profile of the Johansen formation for the simulation scenario 2. The figures on the left side show the saturation profile in the matrix grid cells and the figures on the left side display the saturation maps in the fractures. From the top row towards the bottom row, the saturation profiles are displayed for simulations times 5000, 20000 and 35000[days] respectively.
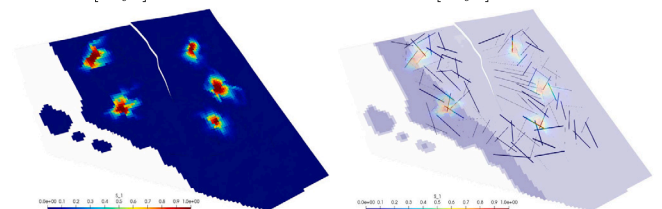
methods (Peters et al., 2010). It is the largest and most complex test case on closed-loop optimization to represent real field management scenarios. The active Brugge field model has 44550 corner-point grid cells, and the main geological features present in the model are a boundary fault and an internal fault. Seven different rock regions with their particular petrophysical properties are distributed throughout the whole model. Thirty wells are included in the field model's well production pattern: 20 producers and 10 injectors (see Fig. 24).
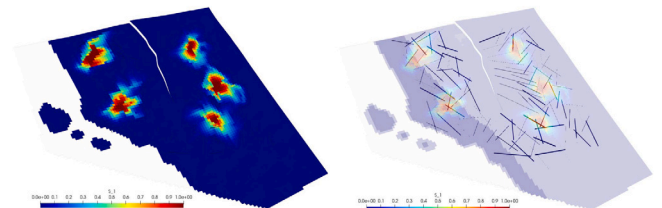
6.5.1. Geological model

The geological structure of the Brugge field contains an east/west elongated half-dome with a boundary fault at its northern edge and an internal fault with a throw at an angle of nearly 20 degrees to

the northern fault edge. The dimensions of the field are approximately 10[km]×3[km]. The original high-resolution model consists of 20 million grid cells, with average cell dimensions of 50[m] × 50[m] × 0.25[m]. In addition to the essential petrophysical properties for reservoir simulation (sedimentary facies, porosity, permeability, net-to-gross, and water saturation), the grid model includes properties measured in real fields (gamma-ray, sonic, bulk density, and neutron porosity). The data were generated at a detailed scale to produce reliable well log data in the thirty wells drilled in the field.

The original high-resolution model was upscaled to a 450000 grid cells model, which established the foundation for all additional reservoir simulations of the reference case. A set of 104 realizations, each
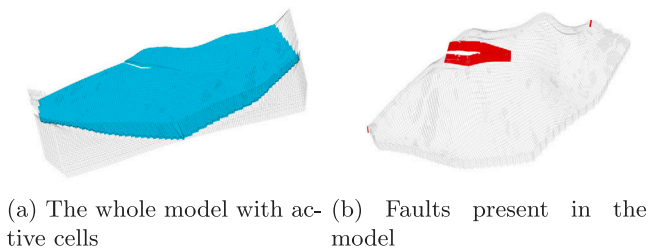
(a) The whole model with active cells   (b) Faults present in the model

Fig. 24. Test case 5: Illustration of the Brugge model. The left graph represents the active section (colored in blue) of the model, and the right figure shows the faults marked with red color. (For interpretation of the references to color in this figure legend, the reader is referred to the web version of this article.)
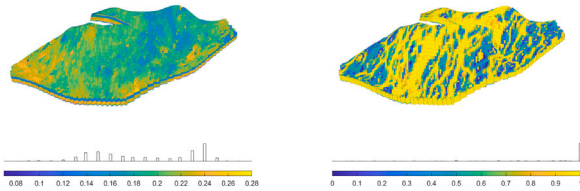

Fig. 25. Test case 5: Porosity and Net-to-gross ratio for the Brugge model. The left graph shows the porosity of the model, and the right one shows the net-to-gross ratio map in the structural model.
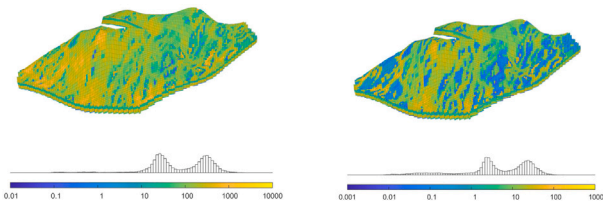

Fig. 26. Test case 5: Permeability map of the Brugge model. The left figure shows the horizontal permeability, and the right figure illustrates the vertical permeability; both are plotted using a logarithmic color scale.

containing 60000 grid cells, was created from the data extracted from the reference case.

All the realizations used the same geological structure of the field. The North Sea Brent-type field was the reference to generate the reservoir zones' rock properties and thicknesses. An alteration of the formations' vertical sequence for the general Brent stratigraphy column (comprising the Broom–Rannoch–Etive–Ness–Tarbert Formations) was made and resulted in that the highly permeable reservoir zone switched locations with the underlying area (less permeable and heterogeneous).

6.5.2. Rock properties

A reservoir model with 60000 grid cells was the reference to create 104 upscaled realizations for the reservoir properties. The properties that contain the realizations are facies, porosity, a diagonal permeability tensor, net-to-gross ratio, and water saturation (see Figs. 25–27).

6.5.3. Simulation results

The following test case from the Brugge model is used to show the pEDFM model's capability in fracture modeling in a synthetic geologically relevant model with the corner-point grid geometry. The reservoir model consists of $138 \times 48 \times 9$ grid cells from which 43474 grid cells are active. Rock properties of the realization available from public data were used in the simulation. A network of 60 fractures is defined in the reservoir domain containing both highly conductive fractures and flow barriers with permeability of $K_{f_{max}} = 10^{-8}$ [m^2] and $K_{f_{min}} = 10^{-20}$ [m^2] respectively. The fracture network consists of 5384 grid cells (in total 48858 grid cells). The well pattern used in this test case was a modified
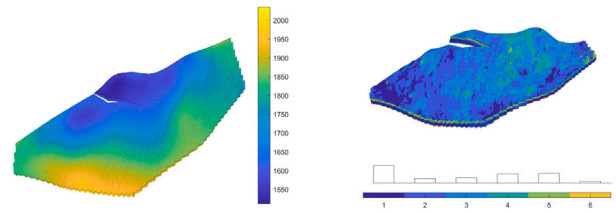

Fig. 27. Test case 5: The depth map and saturation regions of the Brugge field. The left graph displays the depth map, and the right graph represents the rock type distribution displayed in the color bar.
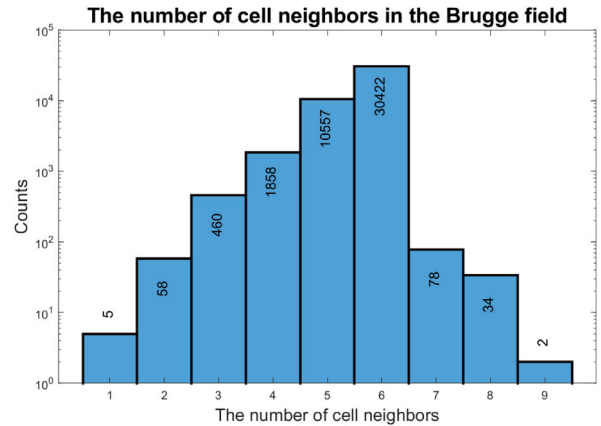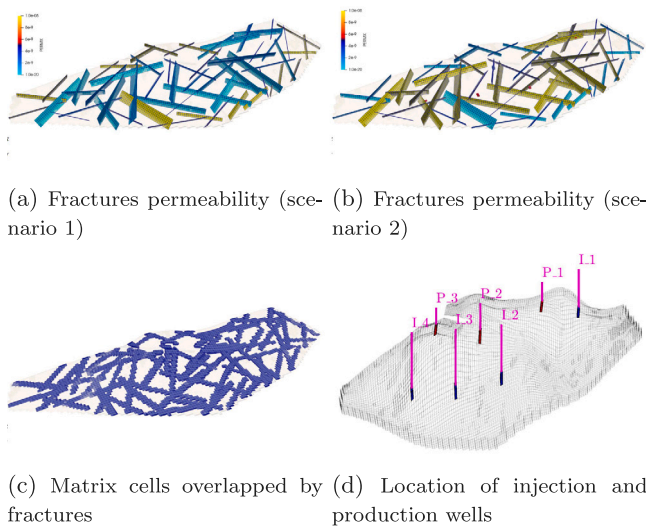

Fig. 28. Test case 5: The Brugge model. The histogram above illustrates the range of neighboring connections between the grid cells of this field. The vertical axis (in logarithmic scale) demonstrates the number of occurrences for a specific number of neighbors for a cell.

version of the original well pattern (with 30 wells) (Peters et al., 2010). Four injection wells with $p_{inj} = 5 \times 10^7$ [Pa] and three production wells with a pressure of $p_{prod} = 1 \times 10^7$ [Pa] were defined in the model. Wells are drilled vertically and through the entire thickness of the reservoir. A histogram is available in Fig. 29 which shows an illustration of the range of the neighboring connections between the matrix grid cells in this model. It can be seen that there are a number of grid cells with more than 6 neighbors due to the non-matching grid topology. This computational model has 66.5 percent of its interfaces as non-planar, and the approximation of the these interfaces into planar quadrilateral interfaces causes 1.23 percent of volume shift in each grid cell, on average. (see Fig. 28)

Two scenarios are created with two different fracture networks including mixed conductivities. The geometries of both fracture networks are identical but the permeability values of the fractures from scenario 1 are inverted for the scenario 2, namely, the highly conductive fractures in the fractures network of scenario 1 act as flow barriers in the 2nd scenario and the flow barriers of scenario 1 are modified to be highly conductive fractures in the scenario 2. Figs. 29(a) and 29(b) show the fracture networks of scenario 1 and scenario 2 respectively. The matrix grid cells overlapped by the fractures are visible in Fig. 19(c).

The pressure and saturation results of the scenario 1 are shown in Figs. 30 and 31 respectively. The pressure results are only shown for the simulation time 5000[days], but the saturation profiles are presented for three time intervals of 2000, 5000 and 10000[days]. The injection wells are surrounded by highly conductive fractures that act as flow channels. As a result, the saturation of the injecting phase is considerably increased in larger distances from the injection phases and the pressure drop around the injection wells is not high.

The results of the 2nd scenario can be seen in Figs. 32 and 33 respectively. The pressure results are only shown for the simulation

(a) Fractures permeability (scenario 1)
(b) Fractures permeability (scenario 2)

(c) Matrix cells overlapped by fractures
(d) Location of injection and production wells

Fig. 29. Test case 5: The Brugge model with 7 wells (4 injectors and 3 producers) and a set of 60 synthetic fractures (with mixed conductivities). The figures on top show the fractures network with different permeabilities for scenario 1 (top left) and scenario 2 (top right). The figure at bottom left illustrates the highlighted matrix cells that are overlapped by the fractures network. And the figure at the bottom right shows the schematics of the injection and production wells.

(a) Pressure in the matrix
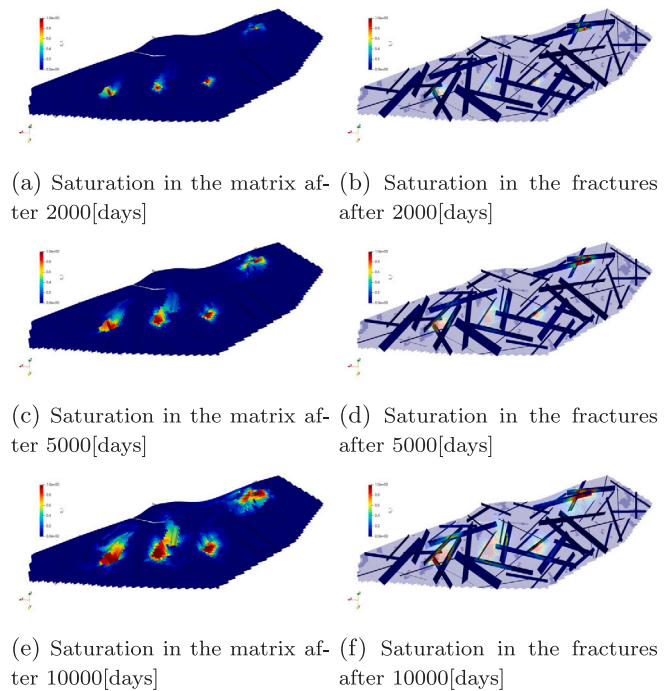(b) Pressure in the fractures
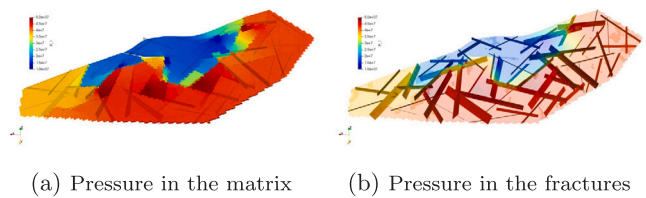
Fig. 30. Test case 5: The pressure profile of the Brugge model for the simulation scenario 1. The figure on the left shows the pressure distribution in the matrix grid cells. The transparency of this figure is increased to make the pressure map in the fractures visible. This map is displayed on the right figure. The results are shown for the simulation time 5000[days].

time 5000[days], but the saturation profiles are presented for three time intervals of 2000, 5000 and 10000[days]. The injection wells are surrounded by flow barriers that restrict the flow. As a result, a high-pressure zone is formed near the wells since the central area of the reservoir is isolated with low permeability fractures. This is followed by a sharp pressure gradient. The saturation displacement is small due to the reservoir's low permeability values and the absence of highly conductive fractures near the wells. The saturation displacement is restricted to the area near the injection wells.

6.6. Test case 6 and 7: Norne field

Norne (Verlo and Hetland, 2008) is an oil and gas field situated in the Norwegian Sea around 80 kilometers north of the Heidrun oil field. The field dimensions are approximately 9[km] × 3[km] and the seawater depth in the area is 9[m]. The field is located in a license awarded region in 1986 and incorporates blocks 6608/10 and 6608/11 (see Fig. 34). Equinor is the current field operator. The expected oil recovery factor is more than 60%, which is very high for an offshore sub-sea oil reservoir.

Subsurface data from the Norne field have been published for research and education purposes thanks to NTNU, Equinor, and partners' initiative. The full simulation model can be obtained through the Open Porous Media (OPM) project (opm-project.org) (Anon, 2020). The Norne field simulation model was the first benchmark case based on

(a) Saturation in the matrix after 2000[days]
(b) Saturation in the fractures after 2000[days]

(c) Saturation in the matrix after 5000[days]
(d) Saturation in the fractures after 5000[days]

(e) Saturation in the matrix after 10000[days]
(f) Saturation in the fractures after 10000[days]

Fig. 31. Test case 5: The saturation profile of the Brugge model for the simulation scenario 1. The figures on the left illustrate the saturation profile in the matrix grid cells and the figures on the right side show the saturation maps in the fractures. From the top row towards the bottom row, the saturation profiles are displayed for simulations times 2000, 5000 and 10000[days] respectively.

(a) Pressure in the matrix
(b) Pressure in the fractures
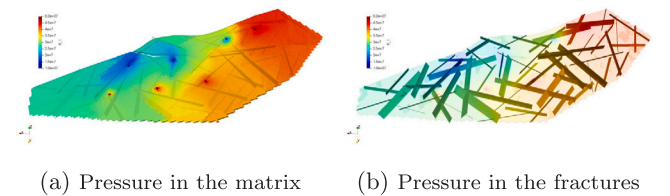
Fig. 32. Test case 5: The pressure profile of the Brugge model for the simulation scenario 2. The figure on the left shows the pressure distribution in the matrix grid cells. The transparency of this figure is increased to make the pressure map in the fractures visible. This map is displayed on the right figure. The results are shown for the simulation time 5000[days].

real field data available to the public. The model is based on the 2004 geological model and consists of 46 × 112 × 22 corner-point grid cells.

6.6.1. Reservoir

The Oil and gas production of Norne is obtained from a Jurassic sandstone, which lies at a depth of 2500 meters below sea level. The original estimation of recoverable resources was 95.2 million cubic meters for oil, mainly in the Ile and Tofte formations, and 13.01 billion cubic meters for gas in the Garn formation.

6.6.2. Field development

The Alve field finding preceded the Norne field's discovery in 1992. The plan for development and operation (PDO) was approved in 1995, and the production started in 1997. The field development infrastructure consists of a production, storage, and offloading vessel (FPSO) attached to sub-sea templates. Water injection is the drive mechanism to produce from the field.

In 2019, Norne FPSO was granted a lifetime extension to increase value creation from the Norne field and its satellite fields, and also, the blow-down of the gas cap in the Not Formation started. In 2020 two
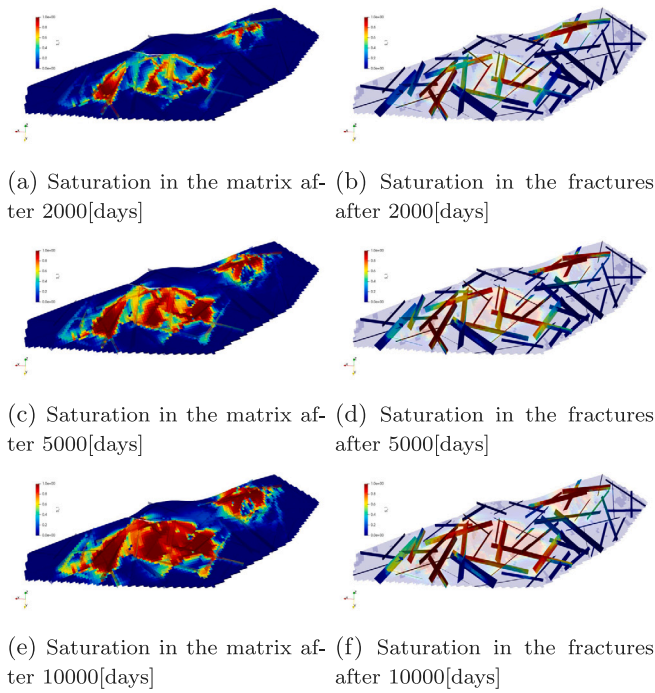
(a) Saturation in the matrix after 2000[days]

(b) Saturation in the fractures after 2000[days]

(c) Saturation in the matrix after 5000[days]

(d) Saturation in the fractures after 5000[days]

(e) Saturation in the matrix after 10000[days]

(f) Saturation in the fractures after 10000[days]

Fig. 33. Test case 5: The saturation profile of the Brugge model for the simulation scenario 2. The figures on the left illustrate the saturation profile in the matrix grid cells and the figures on the right side show the saturation maps in the fractures. From the top row towards the bottom row, the saturation profiles are displayed for simulations times 2000, 5000 and 10000[days] respectively.
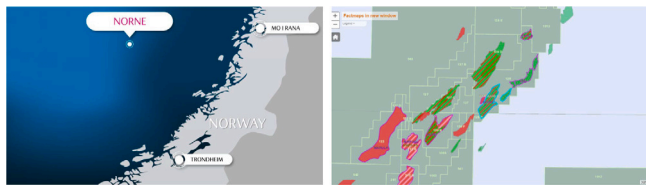

Fig. 34. Test Case 6 and 7: Location of the Norne Field. The left plot shows the field located in the Norwegian sea (source: Equinor), and the right picture shows the location of the licensed blocks (source: Norwegian Petroleum Directorate).
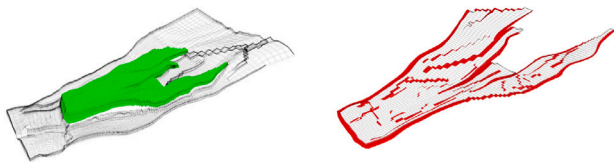

Fig. 35. Test Case 6 and 7: Illustration of the Norne field model. The left graph represents the active section (colored in green) of the model, and the right figure shows the faults marked with red color. (For interpretation of the references to color in this figure legend, the reader is referred to the web version of this article.)

production wells were planned to be drilled in the Ile Formation (see Fig. 35).

6.6.3. Petrophysical data

The field simulation model's petrophysical data consist of porosity, permeability, net-to-gross, and transmissibility multiplier data. Permeability is anisotropic and heterogeneous, with a clear layered structure as expected for a real reservoir field model. The vertical communication is decreased in significant regions of the model by the transmissibility multiplier data that is available, resulting in intermediate layers of the reservoir with permeability values close to zero. The porosity values of
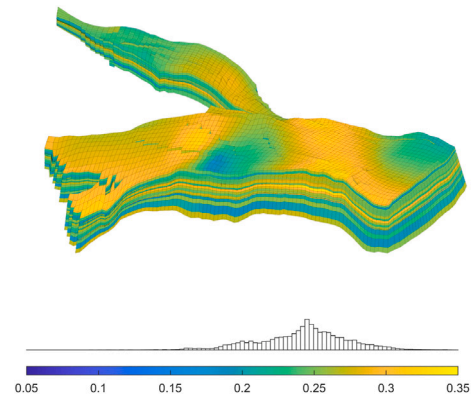

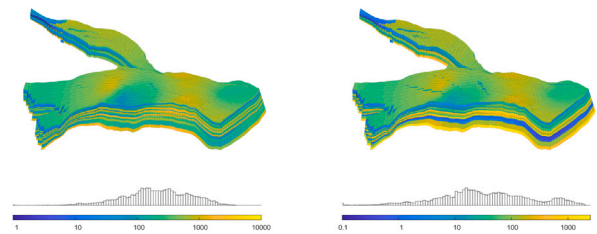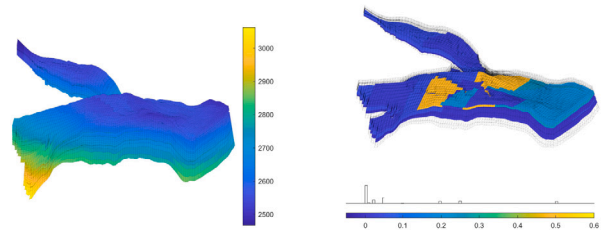**Fig. 36.** Test Case 6 and 7: Porosity map of the Norne Field.

Fig. 37. Test Case 6 and 7: Permeability map of the Norne field. The left figure shows the horizontal permeability, and the right figure displays the vertical permeability; both are plotted using a logarithmic color scale.

(a) The depth map

(b) The map of the transmissibility multipliers

Fig. 38. Test Case 6 and 7: Depth map of the Norne field and the vertical transmissibility multipliers that reduce the vertical communication between the grid cells.

the field are in the interval between 0.094 and 0.347 (see Fig. 36). A considerable percentage of impermeable shale is present in some regions in the model (see Figs. 37–39).

6.6.4. Simulation results of test case 6: Norne with highly conductive fractures

This test case demonstrates the performance of the pEDFM model on the Norne field. The corner-point grid data for this and the following test cases were extracted from the input files of MATLAB Reservoir Simulation Toolbox (MRST) (Lie, 2019).

As explained above, Norne is an oil field located around 80 kilometers north of the Heidrun oil field in the Norwegian Sea (Lie, 2019). As described in the MRST (Lie, 2019), the extent of this oil field is $10\,[\mathrm{Km}] \times 2\,[\mathrm{Km}] \times 100\,[\mathrm{m}]$. The corner-point grid skeleton consists of $46 \times 112 \times 22$ grid cells from which 44915 grid cells are active forming the complex geometrical shape of this oil field. A synthetic network of 15 fractures (designed by the author as a realization) is considered inside this domain. The permeability of the Norne rock matrix in this test case is assumed to be constant at $K_m = 10^{-14}\,[\mathrm{m}^2]$

and the permeability data from the field was not used in this test case. All fractures are highly conductive with a permeability of $K_f = 10^{-8}$ [m^2]. Two injection wells with pressure of $p_{\text{inj}} = 5 \times 10^7$ [Pa] and two production wells with pressure of $p_{\text{prod}} = 1 \times 10^7$ [Pa] are located in the outer skirts of the reservoir as it can be seen on Fig. 39(a). All wells are vertical and perforate the entire thickness of the reservoir. For this test case, the low-enthalpy single-phase geothermal fluid model was used. The input parameters used in this test case are listed in Table 2.

6.6.5. Simulation results of test case 7: Norne with mix-conductive fractures

In this test case, the Norne field model with a skeleton of $46 \times 112 \times 22$ grid cells and a total of 44915 active matrix grid cells is considered. Unlike in test case 6, the real rock properties of the Norne field were used in this test case. A set of 56 synthetic fractures are created and embedded in the reservoir domain which comprises highly conductive fractures and flow barriers with permeability of $K_{f_{max}} = 10^{-8}$ [m^2] and $K_{f_{min}} = 10^{-20}$ [m^2] respectively. The fracture network consists of 2165 grid cells. In total there are 48705 grid cells in this test case. Four injection wells with a $p_{\text{inj}} = 5 \times 10^7$ [Pa] and three production wells with a $p_{\text{prod}} = 1 \times 10^7$ [Pa] were placed in the model. Wells are vertical and drilled through the entire thickness of the model. Fig. 40 demonstrates a histogram with the number of occurrences for a specific number of neighboring connections between the grid cells of this computational domain. The distribution of the counts of the neighboring connections shows that a considerably large number of grid cells have more than 6 neighbors, some with up to 20 neighboring connections which is a result of the non-matching grids. Correct computation of the matrix–fracture connectivities on this domain with such a topological complexity is crucial for the accurate capture of the effect of the embedded fractures and faults on the flow patterns. In this computational model, 56.5 percent of the interfaces are non-planar, and the approximation of the these interfaces into planar quadrilateral interfaces results in a volume shift of 4.45 percent in each grid cell, in average.

Like the test cases in Johansen 6.4 and Brugge 6.5 models, two scenarios are considered for the fracture network used in this test case. In both scenarios, the geometrical properties of the fracture networks are identical. However, the permeability values of the highly conductive fractures and flow barriers from the scenario 1 are inverted in the scenario 2 (see Fig. 41).

The pressure and saturation results of scenario 1 simulation are presented in Figs. 42 and 43 respectively. The pressure results are only shown for simulation time 5000[days], but the saturation profiles are presented for three time intervals of 2000, 5000 and 10000[days]. The injection wells are surrounded by flow barriers that restrict the saturation displacement in the reservoir. The pressure is high in the areas near the wells. These high-pressure areas are an indication that the pEDFM implementation in the corner-point grid geometry is successful in the modeling of the fractures with low conductivities. High pressure drops can be seen at the location of the flow barriers. The increase in saturation is mainly carried out in two parts of the model. These two areas are not isolated from the rest of the model which allows a distribution of the injecting phase through the flow paths.

The results of scenario 2 are shown in Figs. 44 and 45 respectively. In the same manner as for the previous scenario, the pressure results are only shown for the simulation time 5000[days], while the saturation profiles are shown for time intervals of 2000, 5000 and 10000[days]. The injection wells are surrounded by highly conductive fractures that act as flow channels. The pressure is more uniformly distributed. As a result, the effect of high permeable fractures near the injector wells has increased the saturation displacement across larger distances in the domain.
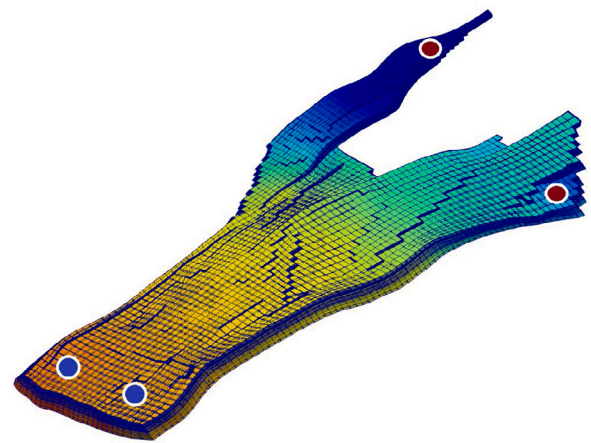
(a) Pressure - Matrix
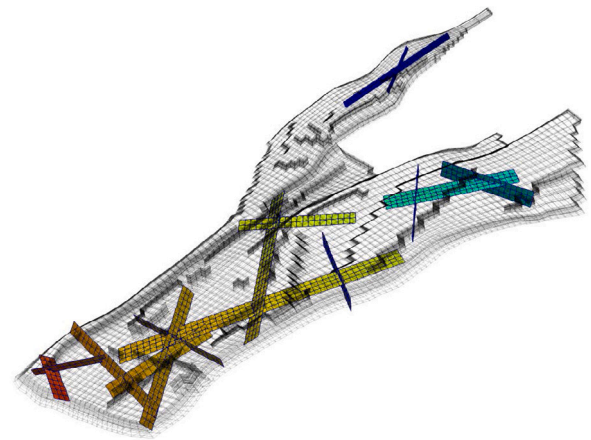
(b) Pressure - Fractures
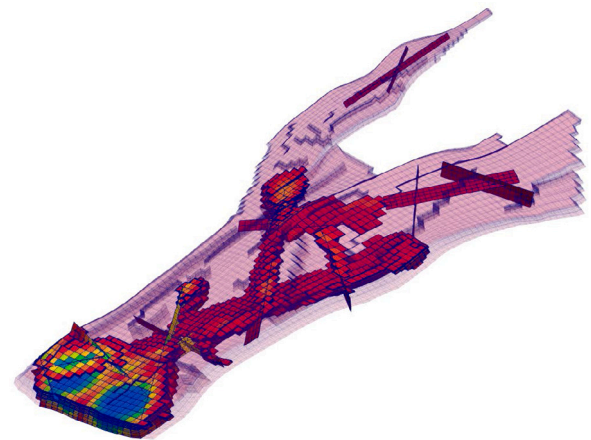
(c) Temperature

Fig. 39. Test case 6: Norne oil field. The Figs. 39(a) and 39(b) show the pressure solutions of the matrix and the embedded fractures. The figure on the bottom row 39(c) visualizes the temperature solution at the same time-step.

7. Conclusions and future work

In this paper, a projection-based embedded discrete fracture model (pEDFM) for corner-point grid (CPG) geometry was developed and presented. This method was used with different fluid models, i.e., for
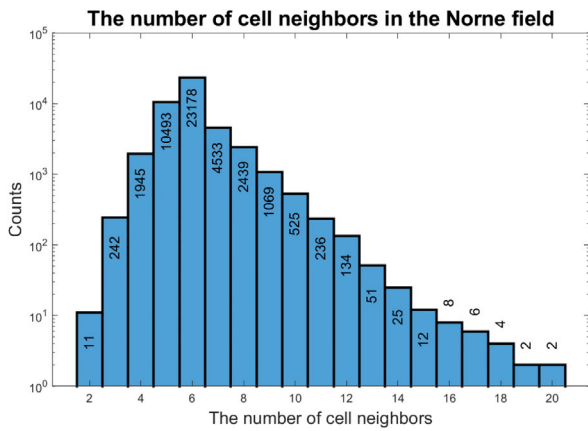
Fig. 40. Test case 6: The Norne field. The histogram above shows a distribution of the number of neighboring connections between the grid cells of this model. The vertical axis shows the number of occurrences (in logarithmic scale). It can be seen that there are grid cells that are connected to more than 6 other cells, with some having up to 20 neighboring connections.
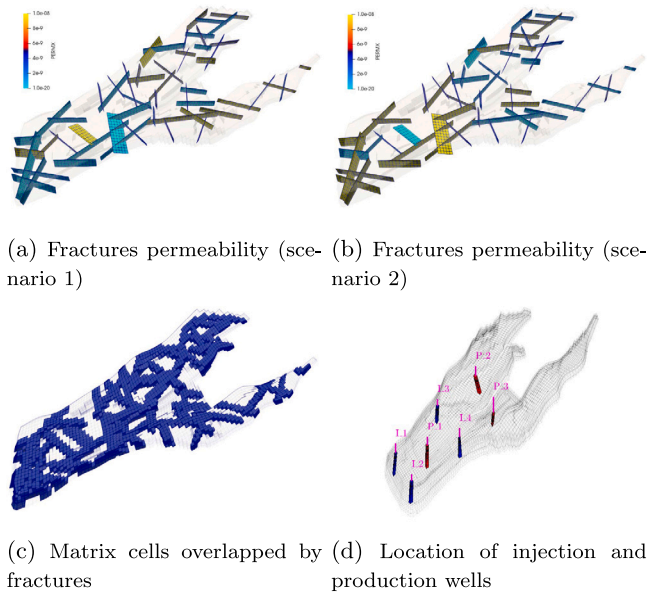

(a) Fractures permeability (scenario 1)

(b) Fractures permeability (scenario 2)

(c) Matrix cells overlapped by fractures

(d) Location of injection and production wells

Fig. 41. Test case 7: The Norne model with 7 wells (4 injectors and 3 producers) and a set of 56 synthetic fractures (with mixed conductivities). The figures on top show the fractures network with different permeabilities for scenario 1 (top left) and scenario 2 (top right). The figure at bottom left illustrates the highlighted matrix cells that are overlapped by the fractures network. And the figure at the bottom right shows the schematics of the injection and production wells.

fully-implicit simulation of isothermal multiphase fluid flow and low-enthalpy single-phase coupled mass-heat flow in fractured heterogeneous porous media. First, the corner-point grid geometry and its discretization approach were briefly described. Afterwards, the pEDFM model (Tene et al., 2017; HosseiniMehr et al., 2020) was extended to account for fully 3D fracture geometries in a generic corner-point grid discrete system. Through a few box-shaped 2D and 3D homogeneous and heterogeneous test cases, the accuracy of the pEDFM on the corner-point grid geometry was briefly compared against the Cartesian grid geometry. The new method presented similar results of satisfactory accuracy in the corner-point grid geometry when compared to a Cartesian grid-geometry. The 3D box-shaped reservoir was then converted into a non-orthogonal gridding system to assess the pEDFM method further.
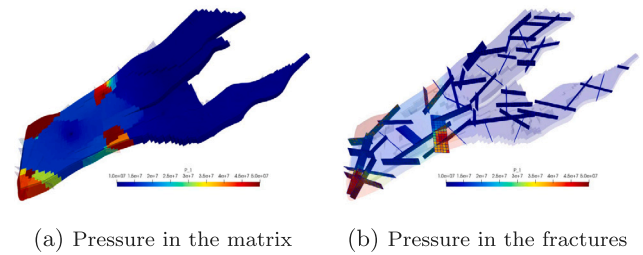

(a) Pressure in the matrix

(b) Pressure in the fractures

Fig. 42. Test case 7: The pressure profile of the Norne model for the simulation scenario 1. The figure on the left shows the pressure distribution in the matrix grid cells. The transparency of this figure is increased to make the pressure map in the fractures visible. This map is displayed on the right figure. The results are shown for simulation time 5000[days].

(a) Saturation in the matrix after 2000[days]

(b) Saturation in the fractures after 2000[days]

(c) Saturation in the matrix after 5000[days]

(d) Saturation in the fractures after 5000[days]

(e) Saturation in the matrix after 10000[days]

(f) Saturation in the fractures after 10000[days]

Fig. 43. Test case 7: The saturation profile of the Norne model for the simulation scenario 1. The figures on the left illustrate the saturation profile in the matrix grid cells and the figures on the right side show the saturation maps in the fractures. From the top row towards the bottom row, the saturation profiles are displayed for simulations times 2000, 5000 and 10000[days] respectively.

Moreover, numerical results were obtained on a number of geologically-relevant test cases. Different scenarios with various synthetic fracture networks were considered for these test cases. These fine-scale simulations allowed for mix-conductivity fractures. It was shown that pEDFM can accurately capture the physical influence of both highly conductive fractures and flow barriers on the flow patterns. The pEDFM in the corner-point grid geometry is found to be a promising technique for increasing the discretization flexibility and enhancing the computational performance while honoring the accuracy. Many geo-models (including ones used in the test cases above) contain millions of grid cells that have complex geometrical alignments to match the positioning of fractures and faults, causing significant
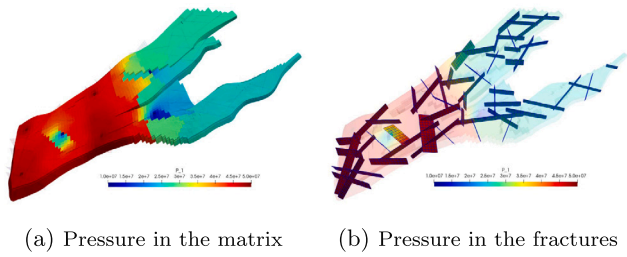
(a) Pressure in the matrix   (b) Pressure in the fractures

Fig. 44. Test case 7: The pressure profile of the Norne model for the simulation scenario 2. The figure on the left shows the pressure distribution in the matrix grid cells. The transparency of this figure is increased to make the pressure map in the fractures visible. This map is displayed on the right figure. The results are shown for simulation time 5000[days].
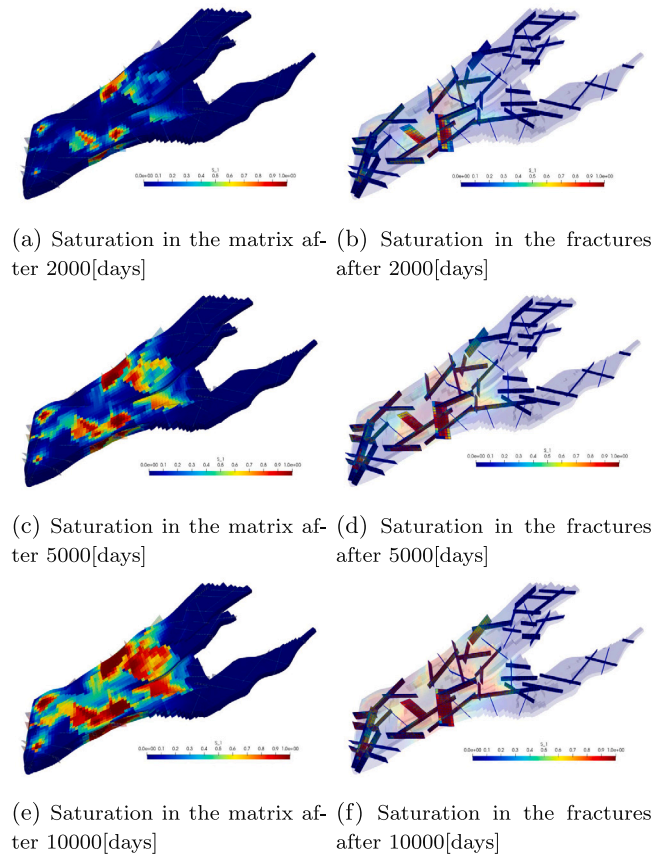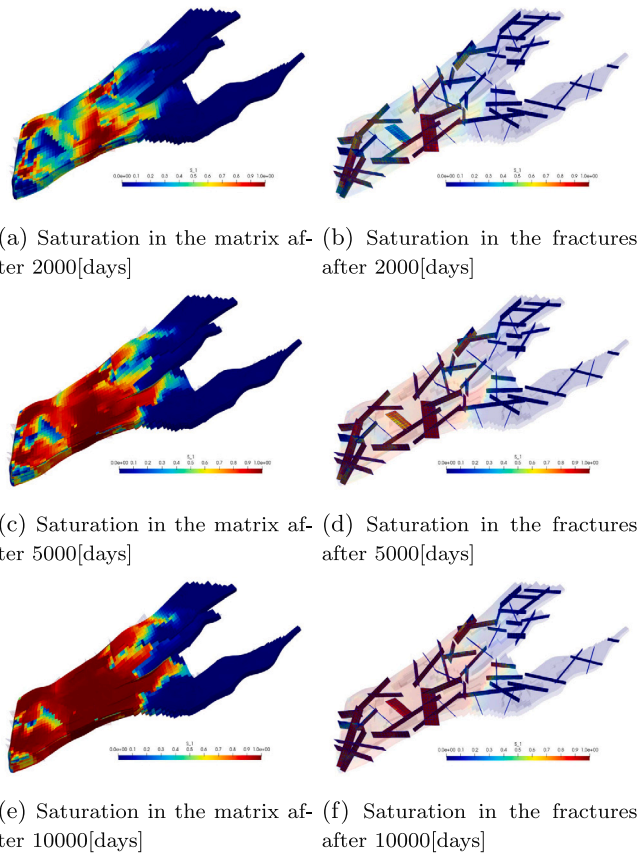

(a) Saturation in the matrix after 2000[days]   (b) Saturation in the fractures after 2000[days]

(c) Saturation in the matrix after 5000[days]   (d) Saturation in the fractures after 5000[days]

(e) Saturation in the matrix after 10000[days]   (f) Saturation in the fractures after 10000[days]

Fig. 45. Test case 7: The saturation profile of the Norne model for the simulation scenario 2. The figures on the left illustrate the saturation profile in the matrix grid cells and the figures on the right side show the saturation maps in the fractures. From the top row towards the bottom row, the saturation profiles are displayed for simulations times 2000, 5000 and 10000[days] respectively.

computational complexity and lack of flexibility especially when taking geomechanical deformation into account. The pEDFM model provides the possibility to avoid the complexity of gridding in such models by explicitly representing the discontinuities such as fractures and faults. In the presence of elastic and (more importantly) plastic deformations, one could only modify the gridding structure of the affected region in the rock matrix, fully independent of the fractures and faults. This advantage results in significant computational gains especially in the realm of poromechanics.

The developments of the pEDFM in the corner-point grid geometry and all the related software implementations of this work are made open source and accessible on https://gitlab.com/DARSim.

CRediT authorship contribution statement

Declaration of competing interest

Acknowledgments

Appendix. Mass and heat conservation for high-enthalpy geothermal systems

In this section, the governing equations of the single-component (water) two-phase (vapor–liquid) flow in high-enthalpy geothermal systems are described. Due to the thermodynamic conditions, the single-component water can exist in either liquid and vapor (steam) phases in high-enthalpy systems. Two sets of equations are considered, i.e., the mass balance and the energy conservation equations. Each set of equations have two subsets for the two phases but are added together and form one set of equations for the entire system, meaning, one mass balance equation and one energy balance equation for all the phases. Expectedly, in low enthalpy-systems, these equations are reduced to single-phase.

A.1. Mass balance equation

Mass balance for phase α for a system with n_α phases reads

$$
\frac{\partial}{\partial t}\left(\phi \sum_{\alpha=1}^{n_\alpha} \rho_\alpha S_\alpha\right)^m - \nabla \cdot \left(\sum_{\alpha=1}^{n_\alpha}\left(\rho_\alpha \lambda_\alpha \cdot \nabla p\right)\right)^m =
$$
$$
\sum_{i=1}^{n_{\text{frac}}} \rho_\alpha q_\alpha^{m,w} + \sum_{\alpha=1}^{n_\alpha}\sum_{i=1}^{n_{\text{frac}}} \rho_\alpha \mathcal{Q}_\alpha^{m,f_i},
$$
$$
\text{on} \quad \Omega_m \subseteq \mathbf{R}^n, \tag{37}
$$

for the rock matrix m and

$$
\frac{\partial}{\partial t}\left(a\,\phi \sum_{\alpha=1}^{n_\alpha} \rho_\alpha S_\alpha\right)^{f_i} - \nabla \cdot \left(a \sum_{\alpha=1}^{n_\alpha}\left(\rho_\alpha \lambda_\alpha \cdot \nabla p\right)\right)^{f_i} =
$$
$$
\sum_{i=1}^{n_{\text{frac}}} \rho_\alpha q_\alpha^{f_i,w} + \sum_{\alpha=1}^{n_\alpha} \rho_\alpha \mathcal{Q}_\alpha^{f_i,m} + \sum_{\alpha=1}^{n_\alpha}\sum_{j=1}^{n_{\text{frac}}} \left(\rho_\alpha \mathcal{Q}_\alpha^{f_i,f_j}\right)_{j\neq i},
$$
$$
\text{on} \quad \Omega_{f_i} \subseteq \mathbf{R}^{n-1}, \tag{38}
$$

for the discrete fracture f_i with aperture a. The superscripts m, f_i and w indicate the rock matrix, the ith fracture and the wells, respectively. Moreover, ϕ is the medium porosity, and λ_α is the phase mobility, i.e. $\lambda_\alpha = \frac{k_{r,\alpha}}{\mu_\alpha}\mathbf{K}$, where $k_{r,\alpha}$ and μ_α are the phase α relative permeability and viscosity. The term $\mathbf{K}$ is the rock absolute permeability which can be a full tensor. In this work we only consider scalar permeability values, i.e., $\mathbf{K} = k\mathbf{I}$ with $\mathbf{I}$ being the identity matrix. Moreover, ρ_α denotes the fluid density and S_α refers to the saturation of phase α. The fluid pressure p is one of the two primary unknowns, and q_α is

the source term (e.g. injection and production wells). The saturation constraint requires summation of all phases to be equal to the unity, i.e., $\sum_{\alpha=1}^{n_\alpha} S_\alpha = 1$. The terms Q_α^{m,f_i} and $Q_\alpha^{f_i,m}$ are the phase flux exchanges between the rock matrix m and the fracture f_i; and, $Q_\alpha^{f_i,f_j}$ is the influx of phase α from the jth fracture to the ith fracture. The mass conservation ensures that $\iiint_V Q_\alpha^{m,f_i} dV = -\iint_{A_{f_i}} Q_\alpha^{f_i,m} dA$ and $\iint_{A_{f_j}} Q_\alpha^{f_i,f_j} dA = -\iint_{A_{f_j}} Q_\alpha^{f_j,f_i} dA$ (Hajibeygi et al., 2011). The volumetric well fluxes are obtained via Peaceman model (Peaceman, 1978) both for matrix and fractures, i.e.,

$$q_\alpha^{m,w} = \frac{WI \cdot \lambda_\alpha^* \cdot (p^w - p^m)}{\Delta V} \tag{39}$$

$$q_\alpha^{f_i,w} = \frac{WI \cdot \lambda_\alpha^* \cdot (p^w - p^{f_i})}{\Delta A}. \tag{40}$$

Here, WI denotes the well productivity index and λ^* is the effective mobility of each phase between the well and the perforating compartment in each medium and is obtained using upwind scheme. In the discrete system for the rock matrix, the control volume is defined as ΔV, and for the lower-dimensional fracture, the control area is defined as ΔA. The volumetric flux exchanges between the rock matrix and the fractures are similarly calculated as

$$Q_\alpha^{m,f_i} = CI^{m,f_i} \cdot \lambda_\alpha^* \cdot (p^{f_i} - p^m)$$
$$Q_\alpha^{m,f_i} = CI^{f_i,m} \cdot \lambda_\alpha^* \cdot (p^m - p^{f_i})$$
$$Q_\alpha^{f_i,f_j} = CI^{f_i,f_j} \cdot \lambda_\alpha^* \cdot (p^{f_j} - p^{f_i}),$$

Where CI is the connectivity index and explained in the next section.

A.2. Energy balance

The energy balance equation for a high-enthalpy multi-phase flow system with the assumption of local equilibrium on the domain reads

$$\frac{\partial}{\partial t}\left((\rho U)_{eff}\right)^m - \nabla \cdot \left(\sum_{\alpha=1}^{n_\alpha}\left(\rho_\alpha h_\alpha \lambda_\alpha \cdot \nabla p\right)\right)^m -$$
$$\nabla \cdot \left(\Lambda_{eff} \cdot \nabla T\right)^m =$$
$$\sum_{i=1}^{n_{\text{frac}}} \rho_\alpha h_\alpha q_\alpha^{m,w} + \sum_{\alpha=1}^{n_\alpha}\sum_{i=1}^{n_{\text{frac}}} \rho_\alpha h_\alpha Q_\alpha^{m,f_i} + \sum_{i=1}^{n_{\text{frac}}} \mathcal{R}^{m,f_i},$$
$$\text{on} \quad \Omega_m \subseteq \mathbf{R}^n, \tag{41}$$

on the rock matrix (m) and

$$\frac{\partial}{\partial t}\left(a(\rho U)_{eff}\right)^{f_i} - \nabla \cdot \left(a\sum_{\alpha=1}^{n_\alpha}\left(\rho_\alpha h_\alpha \lambda_\alpha \cdot \nabla p\right)\right)^{f_i} - \nabla \cdot \left(\Lambda_{eff} \cdot \nabla T\right)^{f_i} =$$
$$\sum_{i=1}^{n_{\text{frac}}} \rho_\alpha h_\alpha q_\alpha^{f_i,w} + \sum_{\alpha=1}^{n_\alpha} \rho_\alpha h_\alpha Q_\alpha^{f_i,m} + \sum_{\alpha=1}^{n_\alpha}\sum_{i=1}^{n_{\text{frac}}}\left(\rho_\alpha h_\alpha Q_\alpha^{f_i,f_j}\right)_{j\neq i} +$$
$$\mathcal{R}^{f_i,m} + \sum_{i=1}^{n_{\text{frac}}}\left(\mathcal{R}^{f_i,f_j}\right)_{j\neq i},$$
$$\text{on} \quad \Omega_{f_i} \subseteq \mathbf{R}^{n-1}, \tag{42}$$

on the lower dimensional fracture (f_i). In these of equations, in addition to the previously defined parameters, h_α is the fluid enthalpy of phase α. The term $(\rho U)_{eff}$ indicates the effective internal energy per unit of mass and is calculated as

$$(\rho U)_{eff} = \phi \sum_{\alpha=1}^{n_\alpha} \rho_\alpha S_\alpha U_\alpha + (1 - \phi)\rho_r U_r, \tag{43}$$

with U_α and U_r being the specific internal energy in fluid (for each phase) and rock respectively. The dependent terms are nonlinear functions of the primary unknowns, and are calculated using constitutive

relations (Coats et al., 1980; Faust et al., 1979). Additionally, Λ_{eff} is the effective thermal conductivity written as

$$\Lambda_{eff}^m = \phi^m \sum_{\alpha=1}^{n_\alpha} S_\alpha \Lambda_\alpha + (1 - \phi^m)\Lambda_r \tag{44}$$

$$\Lambda_{eff}^{f_i} = \phi^{f_i} \sum_{\alpha=1}^{n_\alpha} S_\alpha \Lambda_\alpha + (1 - \phi^{f_i})\Lambda_r$$

Here, Λ_α and Λ_r are the thermal conductivities of phase α and rock, respectively. The conductive heat flux exchanges, i.e., $\mathcal{R}^{m,f_i}$, $\mathcal{R}^{f_i,m}$ (matrix–fracture connectivities) and $\mathcal{R}^{f_i,f_j}$ (fracture–fracture connectivities), are calculated as

$$\mathcal{R}^{m,f_i} = CI^{m,f_i} \cdot \Lambda_{eff}^* \cdot (T^{f_i} - T^m)$$
$$\mathcal{R}^{m,f_i} = CI^{f_i,m} \cdot \Lambda_{eff}^* \cdot (T^m - T^{f_i}) \tag{45}$$
$$\mathcal{R}^{f_i,f_j} = CI^{f_i,f_j} \cdot \Lambda_{eff}^* \cdot (T^{f_j} - T^{f_i}).$$

Here, Λ_{eff}^* is the harmonic average between the two non-neighboring compartments.

In the energy balance equation above, two approaches exist for the choice of the primary unknowns. On one hand, the natural formulation employs pressure p and temperature T as the primary unknowns (called as the P-T formulation as well). On the other hand, the molar formulation can be used where the pressure p and the total fluid enthalpy H are considered as the primary unknowns (also known as p-H formulation). The details for the choice of the primary unknown is available in the literature (Coats et al., 1980; Faust et al., 1979). Please note that the effects of both capillarity (in case of a multiphase flow) and gravity are neglected in all the equations.

A.3. Discretization of the equations and the simulation strategy

The discretization of the nonlinear equations is done using the finite volume method (FVM). The equations are discretized with a two-point-flux-approximation (TPFA) finite-volume scheme in space and a backward (implicit) Euler scheme in time. Independent structured grids are generated for a three-dimensional (3D) porous rock and 2D fracture plates. The discretization is done for each medium. For a corner-point grid geometry, an illustration is presented in Fig. 4.

A.3.1. Mass and heat fluxes

The coupled system of non-linear equations (Eqs. (37)–(38) and (41)–(42)) is discretized by calculating the fluxes. First, the discrete mass fluxes need to be calculated. The mass flux of the phase α between each two neighboring control volumes i and j (inside one medium) using the TPFA scheme can be written as

$$F_{\alpha,ij} = \rho_\alpha^* \frac{k_{r_\alpha}^*}{\mu_\alpha^*} T_{ij}(p_i - p_j). \tag{46}$$

Here, $T_{ij} = \frac{A_{ij}}{d_{ij}} K_{ij}^H$ denotes the transmissibility between the neighboring cells i and j. A_{ij} and d_{ij} are the interface area and the distance between these two cell centers respectively. The term K_{ij}^H is the harmonic average of the two permeabilities. The superscript $*$ indicates that the corresponding terms are evaluated using a phase potential upwind scheme.

Following the EDFM and pEDFM paradigms (Hajibeygi et al., 2011; Tene et al., 2017; HosseiniMehr et al., 2018), the fluxes between a rock matrix cell i and a fracture cell j are modeled as

$$\mathcal{F}_{\alpha,ij}^{m,f} = -\mathcal{F}_{\alpha,ij}^{f,m} = -\rho_\alpha^* \frac{k_{r_\alpha}^*}{\mu_\alpha^*} T_{ij}^{m,f}(p_i^m - p_j^f), \tag{47}$$

In this equation, $T_{ij}^{m,f}$ is the geometrical transmissibility in the mass flux between cell i belonging to the rock matrix m and the element j belonging to the fracture f and it reads

$$T_{ij}^{m,f} = K_{ij}^H \times CI^{m,f}. \tag{48}$$

In the equation above, K_{ij}^H denotes the harmonically averaged permeability between the rock matrix and the overlapping fracture elements. Moreover, $CI_{ij}^{m,f}$ is the connectivity index between the two mentioned overlapping elements. The EDFM and pEDFM model the matrix–fracture connectivity index as

$$CI_{ij}^{m,f} = \frac{A_{ij}^{m,f}}{\langle d \rangle_{ij}}, \tag{49}$$

with $A_{ij}^{m,f}$ being the area fraction of fracture cell j overlapping with the rock matrix cell i (see Fig. 1) and $\langle d \rangle_{ij}$ being the average distance between these two cells (Hajibeygi et al., 2011). The computation of the connectivity index is identical for bot types of fractures (either conductive or impermeable).

Similarly, the flux exchange between intersecting fracture elements i (belonging to fracture f_h) and j (belonging to fracture f_k) is modeled as

$$\mathcal{F}_{\alpha,ij}^{f_h,f_k} = -\mathcal{F}_{\alpha,ij}^{f_k,f_h} = -\rho_\alpha^* \frac{k_{r_\alpha}^*}{\mu_\alpha^*} T_{ij}^{f_h,f_k}(p_i^{f_h} - p_j^{f_k}). \tag{50}$$

Here, $T_{ij}^{f_h,f_k}$ is the geometrical transmissibility in the mass flux between element i in the fracture f_h and the element j in the fracture f_k, which reads

$$T_{ij}^{f_h,f_k} = a K_{ij}^H \frac{CI_{iI_{ij}}^{f_h} \times CI_{jI_{ij}}^{f_k}}{CI_{iI_{ij}}^{f_h} + CI_{jI_{ij}}^{f_k}}. \tag{51}$$

Please note that the geometrical transmissibility $T_{ij}^{f_h,f_k}$ between the two non-neighboring (intersecting) fracture cells is obtained on a lower dimensional formulation. This is needed due to the fact that the intersection between two 2D fracture plates forms a line-segment and the intersection between two 1D fracture line-segments results in a point. Fig. 1 (on the right) visualizes an example of an intersection between two non-neighboring 2D fracture elements. The result of the intersection is a line segment I_{ij} (colored in red) with the average distances from the intersection segment written as $\langle d \rangle_{iI_{ij}}^{f_h} \neq \langle d \rangle_{jI_{ij}}^{f_k}$. This is the reason why these transmissibilities are computed using a harmonic-average formulation as shown above.

At next, the convective and conductive heat fluxes are calculated. The convective heat flux exchange between the neighboring control volumes i and j for each phase α reads

$$\breve{F}_{\alpha,ij} = \frac{\rho_\alpha^* h_\alpha^*}{\mu_\alpha^*} T_{ij}(p_i - p_j). \tag{52}$$

Here, h_α^* is the enthalpy of phase α in fluid determined at the interface between grid cells i and j. Conclusively, $\breve{F}_{\alpha,ij} = h_\alpha^* F_{\alpha,ij}$. The convective heat flux exchange between non-neighboring elements can be obtained via multiplication of their mass flux exchange ($\mathcal{F}_{\alpha,ij}$) by the effective phase enthalpy (h_α^*) determined at the intersection of two overlapping elements, i.e., $\breve{\mathcal{F}}_{\alpha,ij} = h_\alpha^* \mathcal{F}_{\alpha,ij}$.

The conductive heat flux between two neighboring cells i and j (belonging to one medium) is written as

$$G_{ij} = \mathbb{T}_{cond,ij}(T_i - T_j). \tag{53}$$

where, $\mathbb{T}_{cond,ij} = \frac{A_{ij}}{d_{ij}}(\Lambda_{eff})_{ij}^H$ is the transmissibility between grid cells i and j. A_{ij}, d_{ij} and $(\Lambda_{eff})_{ij}^H$ are the interface area, the distance from the cell centers and the harmonic average of the effective conductivity set at the interface between grid cells i and j respectively. Please note that the effective conductivity is calculated via Eq. (44). The conductive heat flux exchange between non-neighboring elements i and j is obtained as

$$\mathcal{G}_{ij}^{m,f} = -\mathcal{G}_{ij}^{f,m} = -\mathbb{T}_{cond,ij}^{m,f}(T_i^m - T_j^f). \tag{54}$$

for matrix–fracture connectivities and

$$\mathcal{G}_{ij}^{f_h,f_k} = -\mathcal{G}_{ij}^{f_k,f_h} = -\mathbb{T}_{cond,ij}^{f_h,f_k}(T_i^{f_h} - T_j^{f_k}). \tag{55}$$

for fracture–fracture connectivities. The conductive heat transmissibilities for matrix–fracture ($\mathbb{T}_{cond,ij}^{m,f}$) and fracture–fracture ($\mathbb{T}_{cond,ij}^{f_h,f_k}$) connectivities are explained later in this section.

A.3.2. Coupling and linearization of the nonlinear equations

Taking the calculated fluxes above into account, the discrete mass balance equations can be written in their residual form as

$$
\left(r_{MB,i}^{n+1} \right)^m = \left(\sum_{\alpha=1}^{n_{ph}} \rho_\alpha q_\alpha^{m,w} \right)_i - \\
\left(\frac{\left(\phi \sum_{\alpha=1}^{n_{ph}} \rho_\alpha S_\alpha \right)_i^{n+1} - \left(\phi \sum_{\alpha=1}^{n_{ph}} \rho_\alpha S_\alpha \right)_i^n}{\Delta t} \right)^m - \\
\left(\sum_{\alpha=1}^{n_{ph}} \left(\sum_{j=1}^{N_n} F_{\alpha,ij} \right) \right)^m - \sum_{\alpha=1}^{n_{ph}} \left(\sum_{k=1}^{n_{frac}} \left(\sum_{j=1}^{N_{f_k}} \mathcal{F}_{\alpha,ij}^{m,f_k} \right) \right), \\
\forall i \in \{1, \dots, N_m\} \tag{56}
$$

for element i in matrix m and

$$
\left(r_{MB,i}^{n+1} \right)^{f_h} = \left(\sum_{\alpha=1}^{n_{ph}} \rho_\alpha q_\alpha^{f_h,w} \right)_i - \\
\left(\frac{\left(a \phi \sum_{\alpha=1}^{n_{ph}} \rho_\alpha S_\alpha \right)_i^{n+1} - \left(a \phi \sum_{\alpha=1}^{n_{ph}} \rho_\alpha S_\alpha \right)_i^n}{\Delta t} \right)^{f_h} - \\
\left(\sum_{\alpha=1}^{n_{ph}} \left(\sum_{j=1}^{N_n} F_{\alpha,ij} \right) \right)^{f_h} - \sum_{\alpha=1}^{n_{ph}} \left(\sum_{j=1}^{N_{f_k}} \mathcal{F}_{\alpha,ij}^{f_h,m} \right) - \\
\sum_{\alpha=1}^{n_{ph}} \left(\sum_{k=1}^{n_{frac}} \left(\sum_{j=1}^{N_{f_k}} \mathcal{F}_{\alpha,ij}^{f_h,f_k} \right) \right), \\
\forall i \in \{1, \dots, N_{f_h}\} \tag{57}
$$

for element i in fracture f_h. Additionally, the discrete energy balance equations are also rewritten as

$$
\left(r_{EB,i}^{n+1} \right)^m = \left(\sum_{\alpha=1}^{n_{ph}} \rho_\alpha h_\alpha q_\alpha^{m,w} \right)_i - \\
\left(\frac{\left((\rho U)_{eff} \right)_i^{n+1} - \left((\rho U)_{eff} \right)_i^n}{\Delta t} \right)^m - \left(\sum_{\alpha=1}^{n_{ph}} \left(\sum_{j=1}^{N_n} \breve{F}_{\alpha,ij} \right) \right)^m - \\
\sum_{\alpha=1}^{n_{ph}} \left(\sum_{k=1}^{n_{frac}} \left(\sum_{j=1}^{N_{f_k}} \breve{\mathcal{F}}_{\alpha,ij}^{m,f_k} \right) \right) - \left(\sum_{j=1}^{N_n} \breve{G}_{ij} \right)^m - \sum_{k=1}^{n_{frac}} \left(\sum_{j=1}^{N_{f_k}} \breve{\mathcal{G}}_{ij}^{m,f_k} \right), \\
\forall i \in \{1, \dots, N_m\} \tag{58}
$$

for element i in matrix m and

$$
\left(r_{EB,i}^{n+1} \right)^{f_h} = \left(\sum_{\alpha=1}^{n_{ph}} \rho_\alpha h_\alpha q_\alpha^{f_h,w} \right)_i - \\
\left(\frac{\left((\rho U)_{eff} \right)_i^{n+1} - \left((\rho U)_{eff} \right)_i^n}{\Delta t} \right)^{f_h} - \left(\sum_{\alpha=1}^{n_{ph}} \left(\sum_{j=1}^{N_n} \breve{F}_{\alpha,ij} \right) \right)^{f_h} - \\
\sum_{\alpha=1}^{n_{ph}} \left(\sum_{j=1}^{N_m} \breve{\mathcal{F}}_{\alpha,ij}^{f_h,m} \right) - \sum_{\alpha=1}^{n_{ph}} \left(\sum_{k=1}^{n_{frac}} \left(\sum_{j=1}^{N_{f_k}} \breve{\mathcal{F}}_{\alpha,ij}^{f_h,f_k} \right) \right) - \\
\left(\sum_{j=1}^{N_n} \breve{G}_{ij} \right)^{f_h} - \sum_{j=1}^{N_m} \breve{\mathcal{G}}_{ij}^{f_h,m} - \sum_{k=1}^{n_{frac}} \left(\sum_{j=1}^{N_{f_k}} \breve{\mathcal{G}}_{ij}^{f_h,f_k} \right), \\
\forall i \in \{1, \dots, N_m\} \tag{59}
$$

for element i in fracture f_h. The full residual vector for each of the mass balance and energy balance equations can be written as

$r^n = [(r^m)^n, (r^{f_1})^n ... (r^{f_{n_{frac}}})^n]^T$ and, where $(r^k)^n$ is the residual vector of medium k at time-step n. p^n is the vector of the pressure unknowns. Depending on the flow model (i.e., the number of the phases and the thermal conditions), the second primary unknown is either the saturation of the injecting phase (S), the temperature (T) or the total fluid enthalpy (H). For a multi-phase flow model in high-enthalpy systems, the second primary unknown is the total fluid enthalpy with the term H^n indicating the vector of the total fluid enthalpy unknowns at time step n. The residual at time-step $n + 1$, namely, r^{n+1}, is a non-linear function of the primary unknowns (p^{n+1} and H^{n+1}). Therefore, at every time-step a Newton–Raphson method is used to solve the non-linear system iteratively, i.e.,

$$r_{MB}^{\nu+1} = r_{MB}^{\nu} + \left.\frac{\partial r_{MB}}{\partial p}\right|^{\nu} \delta p^{\nu+1} + \left.\frac{\partial r_{MB}}{\partial H}\right|^{\nu} \delta H^{\nu+1} = 0 \qquad (60)$$

$$r_{EB}^{\nu+1} = r_{EB}^{\nu} + \left.\frac{\partial r_{EB}}{\partial p}\right|^{\nu} \delta p^{\nu+1} + \left.\frac{\partial r_{EB}}{\partial H}\right|^{\nu} \delta H^{\nu+1} = 0$$

where ν and $\nu + 1$ superscripts denote the current and the next iteration indices. At every Newton's iteration step, the linear-system $\mathbf{J}^{\nu} \delta x^{\nu+1} = -r^{\nu}$ is solved. In this notation, $\mathbf{J}^{\nu}$ is the Jacobian matrix with $\delta x^{\nu+1} = [\delta p, \delta H]^T$. Therefore, the linear system of the equations can be re-illustrated as

$$\underbrace{\begin{pmatrix} \begin{pmatrix} J_{MB,p}^{m,m} & J_{MB,p}^{m,f} \\ J_{MB,p}^{f,m} & J_{MB,p}^{f,f} \end{pmatrix} & \begin{pmatrix} J_{MB,H}^{m,m} & J_{MB,H}^{m,f} \\ J_{MB,H}^{f,m} & J_{MB,H}^{f,f} \end{pmatrix} \\ \begin{pmatrix} J_{EB,p}^{m,m} & J_{EB,p}^{m,f} \\ J_{EB,p}^{f,m} & J_{EB,p}^{f,f} \end{pmatrix} & \begin{pmatrix} J_{EB,H}^{m,m} & J_{EB,H}^{m,f} \\ J_{EB,H}^{f,m} & J_{EB,H}^{f,f} \end{pmatrix} \end{pmatrix}}_{\mathbf{J}^{\nu}}^{\nu} \times$$

$$\underbrace{\begin{pmatrix} \delta p^m \\ \delta p^f \\ \delta H^m \\ \delta H^f \end{pmatrix}}_{\delta x^{\nu+1}}^{\nu+1} = - \underbrace{\begin{pmatrix} r_{MB}^m \\ r_{MB}^f \\ r_{EB}^m \\ r_{EB}^f \end{pmatrix}}_{r^{\nu}}^{\nu} \qquad (61)$$

The convergence at each iteration loop is reached by satisfying the following conditions, i.e.,

$$\left(\frac{\|r_{MB}^{\nu+1}\|_2}{\|r_{MB}^0\|_2} < \epsilon_{(r_{MB})} \quad \vee \quad \frac{\|r_{MB}^{\nu+1}\|_2}{\|rhs_{MB}\|_2} < \epsilon_{(r_{MB})} \right) \quad \wedge$$

$$\left(\frac{\|r_{EB}^{\nu+1}\|_2}{\|r_{EB}^0\|_2} < \epsilon_{(r_{EB})} \quad \vee \quad \frac{\|r_{EB}^{\nu+1}\|_2}{\|rhs_{EB}\|_2} < \epsilon_{(r_{EB})} \right) \quad \wedge \qquad (62)$$

$$\left(\frac{\|\delta p\|_2}{\|p\|_2} < \epsilon_{(p)} \quad \wedge \quad \frac{\|\delta H\|_2}{\|H\|_2} < \epsilon_{(T)} \right)$$

Here, each threshold (ϵ_x) is a user-defined tolerance set initially as input at the beginning of the simulation. Notations $\|r\|_2$ and $\|x\|_2$ are the second norm of the vectors of the residuals and the update of the unknowns. The superscript 0 denotes the value of its corresponding vector at the initial state of the iteration step. Please note that in some systems the condition $\frac{\|r^{\nu+1}\|_2}{\|rhs\|_2} < \epsilon(r)$ can result in a better convergence when compared to $\frac{\|r^{\nu+1}\|_2}{\|r^0\|_2} < \epsilon(r)$ and vice versa. Therefore both conditions are checked and either of them can implicate the convergence signal.

References

Ahmed, R., Edwards, M.G., Lamine, S., Huisman, B.A.H., Pal, M., 2015. Control-volume distributed multi-point flux approximation coupled with a lower-dimensional fracture model. J. Comput. Phys. 284, 462–489.

Anon, 2020. Open porous media (OPM). http://opm-project.org. (Accessed 30 October 2020).

Anon, 2021. Pore-scale modelling and sensitivity analyses of hydrogen-brine multiphase flow in geological porous media. Sci. Rep. 11 (1), 8348. http://dx.doi.org/10.1038/s41598-021-87490-7.

Axelsson, G., Stefansson, V., Xu, Y., 2003. Sustainable management of geothermal resources. In: Proceedings of the International Geothermal Conference. pp. 40–48.

Barenblatt, G., Zheltov, Y., Kochina, I., 1983. Basic concepts in the theory of seepage of homogeneous fluids in fissurized rocks. J. Appl. Math. Mech. 5 (24), 1286–1303.

Berkowitz, B., 2002. Characterizing flow and transport in fractured geological media: A review. Adv. Water Resour. 25 (8–12), 861–884.

Bosma, S.B.M., Hajibeygi, H., Tene, M., Tchelepi, H.A., et al., 2017. Multiscale finite volume method for discrete fracture modeling with unstructured grids. SPE Reserv. Simul. Conf. 351, 145–164. http://dx.doi.org/10.2118/182654-MS.

Burnell, J., Clearwater, E., A., C., Kissling, W., OSullivan, J., OSullivan, M., Yeh, A., 2012. Future directions in geothermal modelling. In: 34rd New Zealand Geothermal Workshop. pp. 19–21.

Burnell, J., OSullivan, M., OSullivan, J., Kissling, W., Croucher, A., Pogacnik, J., Pearson, S., Caldwell, G., Ellis, S., Zarrouk, S., Climo, M., 2015. Geothermal supermodels: the next generation of integrated geophysical, chemical and flow simulation modelling tools. In: World Geothermal Congress. pp. 19–21.

Class, H., Ebigbo, A., Helmig, R., Dahle, H.K., Nordbotten, J.M., Celia, M.A., Audigane, P., Darcis, M., Ennis-King, J., Fan, Y., et al., 2009. A benchmark study on problems related to co_2 storage in geologic formations. Comput. Geosci. 13 (4), 409–434.

Coats, K.H., et al., 1980. An equation of state compositional model. Soc. Petrol. Eng. J. 20 (05), 363–376.

Dietrich, P., Helmig, R., Sauter, M., Hotzl, H., Kongeter, J., Teutsch, G., 2005. Flow and Transport in Fractured Porous Media. Springer.

Ding, Y., Lemonnier, P., 1995. Use of corner point geometry in reservoir simulation. In: SPE International Oil and Gas Conference and Exhibition in China, vol. All Days, http://dx.doi.org/10.2118/29933-MS, SPE-29933-MS.

Eigestad, G., Dahle, H., Hellevang, B., Riis, F., Johansen, W., Tian, E., 2009. Geological modeling and simulation of CO2 injection in the Johansen formation. Comput. Geosci. 13 (1), 435–450. http://dx.doi.org/10.1007/s10596-009-9153-y.

Eiken, O., Ringrose, P., Hermanrud, C., Nazarian, B., Torp, T.A., Høier, L., 2011. Lessons learned from 14 years of CCS operations: Sleipner, in Salah and Snøhvit. Energy Procedia 4, 5541–5548. http://dx.doi.org/10.1016/j.egypro.2011.02.541, 10th International Conference on Greenhouse Gas Control Technologies. URL https://www.sciencedirect.com/science/article/pii/S1876610211008204.

Faust, C.R., Mercer, J.W., 1979. Geothermal reservoir simulation: 1. Mathematical models for liquid-and vapor-dominated hydrothermal systems. Water Resour. Res. 15 (1), 23–30.

Flemisch, B., Berre, I., Boon, W., Fumagalli, A., Schwenck, N., Scotti, A., Stefansson, I., Tatomir, A., 2018. Benchmarks for single-phase flow in fractured porous media. Adv. Water Resour. 111, 239–258. http://dx.doi.org/10.1016/j.advwatres.2017.10.036, URL https://www.sciencedirect.com/science/article/pii/S0309170817300143.

Fumagalli, A., Pasquale, L., Zonca, S., Micheletti, S., 2016. An upscaling procedure for fractured reservoirs with embedded grids. Water Resour. Res. 52 (8), 6506–6525.

Gan, Q., Elsworth, D., 2016. Production optimization in fractured geothermal reservoirs by coupled discrete fracture network modeling. Geothermics 62, 131–142.

Garipov, T.T., Karimi-Fard, M., Tchelepi, H.A., 2016. Discrete fracture model for coupled flow and geomechanics. Comput. Geosci. 20 (1), 149–160. http://dx.doi.org/10.1007/s10596-015-9554-z.

Geiger-Boschung, S., Matthäi, S.K., Niessner, J., Helmig, R., 2009. Black-oil simulations for three-component, three-phase flow in fractured porous media. SPE J. 14 (02), 338–354. http://dx.doi.org/10.2118/107485-PA.

GeoQuest, S., 2014. ECLIPSE reference manual. Schlumberger, Houston, Texas.

Gholizadeh Doonechaly, N., Abdel Azim, R., Rahman, S., 2016a. Evaluation of recoverable energy potential from enhanced geothermal systems: a sensitivity analysis in a poro-thermo-elastic framework. Geofluids 16 (3), 384–395.

Gholizadeh Doonechaly, N., Abdel Azim, R.R., Rahman, S.S., 2016b. A study of permeability changes due to cold fluid circulation in fractured geothermal reservoirs. Groundwater 54 (3), 325–335.

Hajibeygi, H., Karvounis, D., Jenny, P., 2011. A hierarchical fracture model for the iterative multiscale finite volume method. J. Comput. Phys. 230 (24), 8729–8743.

Harris, C., Jackson, S., Espie, T., Jones, A., Krevor, S., Muggeridge, A., 2021. The impacts of heterogeneity on co_2 capillary trapping within the captain sandstone-a core to field scale study.. Available at SSRN 3812256.

Heinemann, N., Scafidi, J., Pickup, G., Thaysen, E., Hassanpouryouzband, A., Wilkinson, M., Satterley, A., Booth, M., Edlmann, K., Haszeldine, R., 2021. Hydrogen storage in saline aquifers: The role of cushion gas for injection and production. Int. J. Hydrogen Energy 46 (79), 39284–39296. http://dx.doi.org/10.1016/j.ijhydene.2021.09.174, URL https://www.sciencedirect.com/science/article/pii/S0360319921037277.

HosseiniMehr, M., Cusini, M., Vuik, C., Hajibeygi, H., 2018. Algebraic dynamic multilevel method for embedded discrete fracture model (F-ADM). J. Comput. Phys. 373, 324–345.

HosseiniMehr, M., Vuik, C., Hajibeygi, H., 2020. Adaptive dynamic multilevel simulation of fractured geothermal reservoirs. J. Comput. Phys. X 7, 100061.

Jansen, J.-D., Brouwer, D., Naevdal, G., Van Kruijsdijk, C., 2005. Closed-loop reservoir management. First Break 23 (1), 43–48.

Jiang, J., Younis, R.M., 2016. Hybrid coupled discrete-fracture/matrix and multicontinuum models for unconventional-reservoir simulation. SPE J. 21 (03), 1009–1027. http://dx.doi.org/10.2118/178430-PA.

Jiang, J., Younis, R.M., 2017. An improved projection-based embedded discrete fracture model (pEDFM) for multiphase flow in fractured reservoirs. Adv. Water Resour. 109, 267–289. http://dx.doi.org/10.1016/j.advwatres.2017.09.017, URL https://www.sciencedirect.com/science/article/pii/S0309170817304657.

Karimi-Fard, Durlofsky, L., Aziz, K., 2004. An efficient discrete-fracture model applicable for general-purpose reservoir simulators. SPE J. 227–236.

Karvounis, D.C., 2013. Simulations of Enhanced Geothermal Systems with an Adaptive Hierarchical Fracture Representation (Ph.D. thesis). ETH Zurich.

Kazemi, H., Merrill, L., Porterfield, K., Zeman, P., 1996. Numerical simulation of water-oil flow in naturally fractured reservoirs. SPE J. (5719), 317–326.

Kumar, K., List, F., Pop, I.S., Radu, F.A., 2020. Formal upscaling and numerical validation of unsaturated flow models in fractured porous media. J. Comput. Phys. 407, 109138. http://dx.doi.org/10.1016/j.jcp.2019.109138, URL https://www.sciencedirect.com/science/article/pii/S0021999119308435.

Leal, A.M.M., Kulik, D.A., Smith, W.R., Saar, M.O., 2017. An overview of computational methods for chemical equilibrium and kinetic calculations for geochemical and reactive transport modeling. Pure Appl. Chem. 89 (5), 597–643.

Lee, S., Jensen, C., Lough, M., 1999. An efficient finite difference model for flow in a reservoir with multiple length-scale fractures. SPE ATCE.

Lee, S., Lough, M., Jensen, C., 2001. Hierarchical modeling of flow in naturally fractured formations with multiple length scales. Water Resour. Res. 37 (3), 443–455.

Li, L., Lee, S.H., 2008. Efficient field-scale simulation of black oil in naturally fractured reservoir through discrete fracture networks and homogenized media. SPE Reserv. Eval. Eng. 750–758.

Li, L., Voskov, D., 2021. A novel hybrid model for multiphase flow in complex multi-scale fractured systems. J. Pet. Sci. Eng. 203, 108657. http://dx.doi.org/10.1016/j.petrol.2021.108657, URL https://www.sciencedirect.com/science/article/pii/S092041052100317X.

Lie, K.-A., 2019. An Introduction to Reservoir Simulation using MATLAB/GNU Octave: User Guide for the MATLAB Reservoir Simulation Toolbox (MRST). Cambridge University Press.

Lie, K.-A., Mykkeltvedt, T.S., Møyner, O., 2020. A fully implicit WENO scheme on stratigraphic and unstructured polyhedral grids. Comput. Geosci. 24 (2), 405–423. http://dx.doi.org/10.1007/s10596-019-9829-x, URL https://doi.org/10.1007/s10596-019-9829-x.

Moinfar, A., Varavei, A., Sepehrnoori, K., Johns, R.T., 2013. Development of an efficient embedded discrete fracture model for 3D compositional reservoir simulation in fractured reservoirs. SPE J. 19 (02), 289–303. http://dx.doi.org/10.2118/154246-PA, arXiv:https://onepetro.org/SJ/article-pdf/19/02/289/2099537/spe-154246-pa.pdf.

Moinfar, A., Varavei, A., Sepehrnoori, K., Johns, R.T., 2014. Development of an efficient embedded discrete fracture model for 3D compositional reservoir simulation in fractured reservoirs. SPE J. 19, 289–303.

Morel, F., Morgan, J., 1972. Numerical method for computing equilibriums in aqueous chemical systems. Environ. Sci. Technol. 6 (1), 58–67.

Newman, W.M., 1979. Principles of Interactive Computer Graphics. Tech. rep..

OSullivan, M.J., Pruess, K., Lippmann, M.J., 2001. State of the art of geothermal reservoir simulation. Geothermics 30 (4), 395–429.

Peaceman, D.W., 1978. Interpretation of well-block pressures in numerical reservoir simulation. SPE J. 18 (3), 183–194.

Peters, L., Arts, R., Brouwer, G., 2010. Results of the Brugge benchmark study for flooding optimization and history matching. SPE Reserv. Eval. Eng. 294–295, 391–405. http://dx.doi.org/10.2118/119094-PA.

Ponting, D.K., 1989. Corner point geometry in reservoir simulation. In: ECMOR I-1st European Conference on the Mathematics of Oil Recovery. European Association of Geoscientists & Engineers, cp—-234.

Reichenberger, V., Jakobs, H., Bastian, P., Helmig, R., 2006. A mixed-dimensional finite volume method for two-phase flow in fractured porous media. Adv. Water Resour. 29, 1020–1036.

Rossi, E., Kant, M.A., Madonna, C., Saar, M.O., von Rohr, P.R., 2018. The effects of high heating rate and high temperature on the rock strength: Feasibility study of a thermally assisted drilling method. Rock Mech. Rock Eng.

Ruprecht, C., Pini, R., Falta, R., Benson, S., Murdoch, L., 2014. Hysteretic trapping and relative permeability of co_2 in sandstone at reservoir conditions. Int. J. Greenh. Gas Control 27, 15–27.

Salimzadeh, S., Grandahl, M., Medetbekova, M., Nick, H., 2019. A novel radial jet drilling stimulation technique for enhancing heat recovery from fractured geothermal reservoirs. Renew. Energy 139, 395–409.

Salimzadeh, S., Nick, H., 2019. A coupled model for reactive flow through deformable fractures in enhanced geothermal systems. Geothermics 81, 88–100.

Sandve, T., Berre, I., Nordbotten, J., 2012. An efficient multi-point flux approximation method for discrete fracture-matrix simulations. J. Comput. Phys. 231 (9), 3784–3800. http://dx.doi.org/10.1016/j.jcp.2012.01.023, URL https://www.sciencedirect.com/science/article/pii/S0021999112000447.

Shah, S., Moyner, O., Tene, M., Lie, K.-A., Hajibeygi, H., 2016. The multiscale restriction smoothed basis method for fractured porous media (F-MsRSB). J. Comput. Phys. 318, 36–57. http://dx.doi.org/10.1016/j.jcp.2016.05.001, URL https://www.sciencedirect.com/science/article/pii/S0021999116301267.

Tene, M., Bosma, S.B.M., Kobaisi, M.S.A., Hajibeygi, H., 2017. Projection-based embedded discrete fracture model (pEDFM). Adv. Water Resour. 105, 205–216. http://dx.doi.org/10.1016/j.advwatres.2017.05.009, URL http://www.sciencedirect.com/science/article/pii/S0309170817300994.

Verlo, S.B., Hetland, M., 2008. Development of a Field Case With Real Production and 4D Data From The Norne Field as a Benchmark Case for Future Reservoir Simulation Model Testing (MSc thesis). Norwegian University of Science and Technology, Trondheim, Norway.

Wang, Y., Vuik, C., Hajibeygi, H., 2021. Analysis of hydrodynamic trapping interactions during full-cycle injection and migration of CO2 in deep saline aquifers. Adv. Water Resour. 104073. http://dx.doi.org/10.1016/j.advwatres.2021.104073, URL https://www.sciencedirect.com/science/article/pii/S0309170821002256.

Warren, J., Root, P., 1963. The behavior of naturally fractured reservoirs. SPE J. 245–255.

Wong, Z.Y., Horne, R.N., Tchelepi, H.A., 2018. Sequential implicit nonlinear solver for geothermal simulation. J. Comput. Phys. 368, 236–253. http://dx.doi.org/10.1016/j.jcp.2018.04.043.

Xu, Y., Sepehrnoori, K., 2019. Development of an embedded discrete fracture model for field-scale reservoir simulation with complex corner-point grids. SPE J. 24 (04), 1552–1575. http://dx.doi.org/10.2118/195572-PA, arXiv:https://onepetro.org/SJ/article-pdf/24/04/1552/2118111/spe-195572-pa.pdf.